Momentum decomposition of the pressure field

Citation for the original published paper (version of record):
Zhu, T., Xia, C., Pang, J. et al (2026). Momentum decomposition of the pressure field. PHYSICAL REVIEW FLUIDS, 11(4). http://dx.doi.org/10.1103/bbyr-wqyv

PHYSICAL REVIEW FLUIDS **11**, 044608 (2026)

Momentum decomposition of the pressure field

Taihang Zhu,[1,2,*] Chao Xia,[1,3] Jiabin Pang,[1] Olivier Cadot,[4] and Jonathan F. Morrison[2]
[1]*Shanghai Automotive Wind Tunnel Center, School of Automotive Studies,*
Tongji University, Shanghai 201804, China
[2]*Department of Aeronautics, Imperial College London, London SW7 2AZ, United Kingdom*
[3]*Department of Mechanics and Maritime Sciences, Chalmers University of Technology,*
Gothenburg 412 96, Sweden
[4]*School of Engineering, University of Liverpool, Liverpool L69 3GH, United Kingdom*

(Received 30 May 2025; accepted 1 April 2026; published 24 April 2026)

The generative mechanism of the pressure field is fundamental in turbulence research and flow control, especially when subject to turbulent separation at high Reynolds numbers. To this end, we propose a physics-based framework—momentum decomposition of the pressure field—which uses the momentum equations to decompose the spatial pressure gradient into quantifiable momentum budgets. Each momentum budget corresponds to a distinct physical mechanism, enabling a rigorous decomposition and quantitative evaluation of the inherent mechanisms governing pressure generation. Incorporating results of a direct numerical simulation of laminar cylinder flow, this method is first demonstrated, after which the three-dimensional large eddy simulation results of a complex turbulent bluff body wake at $\mathrm{Re}_D = 1.88 \times 10^5$ are analyzed with a comparison of flow control. In the near wake, the bulk of low pressure originates from the streamwise convection of the centripetal flow outside the wake, which manifests as a streamline curvature effect from the term $\overline{u}\partial\overline{v}/\partial x$, while the pressure variation inside the wake receives main contributions from Reynolds stresses. Under flow control, due to the streamline curvature modification near the base edge, the pulsed jet produces favorable pressure gradients from the mean flow term $\overline{u}\partial\overline{v}/\partial x$ contributing to the bulk of base-pressure recovery. Overall, the proposed framework provides a fundamental flow diagnostic tool and a rigorous foundation for designing and analyzing flow control strategies, since pressure control can be rationally linked to the momentum budgets manipulation, generally applicable to flow regimes governed by the Navier-Stokes equations.

DOI: 10.1103/bbyr-wqyv

I. INTRODUCTION

The turbulent wake formed by flow separation, as a universal phenomenon occurring in a wide range of fluid flows, is a classical problem that has been studied extensively over the past 150 years. From the D'Alembert paradox three centuries ago to the more recent models [1–6], it has been challenging to mathematically model the bluff body wake and predict drag, with the main uncertainties coming from the pressure field, or in particular, the base pressure on the rear

---

[*] Contact author: taihang_zhu@tongji.edu.cn

of the body facing the separated region. The reason is the lack of a universal theory about the wake contribution to this pressure field due to the intricate combination of flow separation, local and global instabilities, recirculating flow, and turbulence—irrespective of the body geometry. Successful attempts have been carried out with the models by Roshko [5] and Balachandar *et al.* [6], which relate the base-pressure coefficient to the shape of the mean separation delimiting the so-called recirculating bubble and key Reynolds stresses. However, these models are generally constrained to two-dimensional (2D) analyses on a single plane of simplified geometries, and the three-dimensional flow and the pressure variation in the wake are not fully considered. In this work, we propose a rigorous decomposition method to analyze the pressure source in the wake and base pressure, with and without flow control techniques. Different from the previous decomposition methods focusing on low-dimensional modeling [7–12], the decomposition method presented here analyses the pressure effect of turbulent flow by means of decomposing it into contributions from acceleration terms of the momentum equation, thereby transferring the pressure gradient into physically interpretable momentum budgets from the Navier-Stokes (NS) equation or Reynolds-average Navier-Stokes (RANS) equation.

The turbulent bluff body wake involves complex and unsteady coherent structures, considering the spatial-temporal scales of the motion involved and the stochastic wake meandering [13–19]. The inlet flow around an axisymmetric body undergoes symmetry-breaking flow separation near the trailing edge, forming unsteady asymmetric global instabilities of vortex shedding at Strouhal number (based on base diameter D and inlet velocity U_∞) $St_D = 0.2$, corresponding to azimuthal wave number $m = \pm 1$ [15,20,21]. At a timescale of ≈ 100 times higher ($tU_\infty/D \approx 500$), the stochastic meandering of vortex shedding plane in an infinite number of azimuthal positions leads to the multistability of the turbulent axisymmetric body wake [15,20,21], or bistability in rectangular-sectioned bluff body wake due to two-preferable symmetry-breaking locations [17,19,22,23]. Besides these symmetry-breaking processes with $m = \pm 1$, a global streamwise pulsation of the recirculation bubbles with $m = 0$ occurs at $St_D = 0.06$. Near the subharmonic of the vortex shedding ($St_D = 0.1$), the squeezing of the wake from two sides results in a global mode with $m = \pm 2$ [20]. The recent conditional proper orthogonal decomposition (CPOD) by Zhu *et al.* [24] illustrates that in the quasistable wake states, the low-dimensional coherent structures are asymmetric, resembling the unstable eigenmodes in the laminar wake [25].

Despite the challenges imposed by these complicated wake dynamics, several flow control methods have been proposed to manipulate the turbulent wake for favorable real-world applications [14,26,27]. For the purpose of drag reduction, the periodic pulsed jet has been studied vigorously to recover the base pressure of the turbulent wake [21,28–34]. The high-frequency pulsed jet employed by Lambert *et al.* [35–37] indicates effective controls of the wake symmetry and, thereby, the aerodynamic loads of the bluff body. More recently, traveling jets are proposed to actively control the unsteady coherent structures of the turbulent wake, achieving 62% base-pressure recovery in the optimal control result [38]. However, as a complex flow phenomenon with multiple low-dimensional modes and coherent structures coupled together [13,39–41], effective flow control methods often result in multiple responses from the turbulent wake, whether beneficial or harmful for the control target. Consequently, it is desirable to analyze the contribution of the turbulent flow to the pressure field, thereby analyzing the source of pressure force and clarifying the mechanism of flow control.

In this work, we focus on a fundamental problem of the turbulent wake: the correlation between the pressure field (base pressure) and the velocity field, with and without flow control. By proposing a rigorous decomposition method based on the momentum equation, these problems are decomposed into physically interpretable and quantitatively assessable acceleration terms known as momentum budgets, usually with very few dominating ones. The proposed method is also largely model-adaptive and insensitive to the flow condition, widely applicable to different geometries and flows, with the condition that the NS equations are valid.

The article is organized as follows: In Sec. II, a description of the momentum decomposition method is given. Section III presents a brief description of the direct numerical simulation (DNS) and large eddy simulation (LES) data used in the current study. a demonstration of the momentum decomposition in the laminar cylinder flow is given in Sec. IV, and the results in Sec. V focus on the pressure field and base-pressure decomposition of the turbulent wake, followed by flow control mechanism and flow control scenarios. Finally, conclusions are given in Sec. VI.

II. DECOMPOSITION METHOD

The relationship between time-averaged pressure $\overline{p}$ and the velocity field of incompressible flow is governed by the three-dimensional (3D) RANS equations, which shows that in the Cartesian coordinate system [Fig. 3(a)], the mean pressure gradient components, streamwise $\partial\overline{p}/\partial x$, lateral $\partial\overline{p}/\partial y$, and perpendicular $\partial\overline{p}/\partial z$, can be calculated with momentum budgets including the mean velocity terms, the Reynolds stress terms, and the viscous terms, given by

$$\frac{\partial \overline{p}}{\partial x} = -\rho\left[\overline{u}\frac{\partial \overline{u}}{\partial x} + \overline{v}\frac{\partial \overline{u}}{\partial y} + \overline{w}\frac{\partial \overline{u}}{\partial z}\right] - \rho\left[\frac{\partial \overline{u'u'}}{\partial x} + \frac{\partial \overline{u'v'}}{\partial y} + \frac{\partial \overline{u'w'}}{\partial z}\right] + \mu\left[\frac{\partial^2 \overline{u}}{\partial x^2} + \frac{\partial^2 \overline{u}}{\partial y^2} + \frac{\partial^2 \overline{u}}{\partial z^2}\right], \tag{1a}$$

$$\frac{\partial \overline{p}}{\partial y} = -\rho\left[\overline{u}\frac{\partial \overline{v}}{\partial x} + \overline{v}\frac{\partial \overline{v}}{\partial y} + \overline{w}\frac{\partial \overline{v}}{\partial z}\right] - \rho\left[\frac{\partial \overline{u'v'}}{\partial x} + \frac{\partial \overline{v'v'}}{\partial y} + \frac{\partial \overline{v'w'}}{\partial z}\right] + \mu\left[\frac{\partial^2 \overline{v}}{\partial x^2} + \frac{\partial^2 \overline{v}}{\partial y^2} + \frac{\partial^2 \overline{v}}{\partial z^2}\right], \tag{1b}$$

$$\frac{\partial \overline{p}}{\partial z} = -\rho\left[\overline{u}\frac{\partial \overline{w}}{\partial x} + \overline{v}\frac{\partial \overline{w}}{\partial y} + \overline{w}\frac{\partial \overline{w}}{\partial z}\right] - \rho\left[\frac{\partial \overline{u'w'}}{\partial x} + \frac{\partial \overline{v'w'}}{\partial y} + \frac{\partial \overline{w'w'}}{\partial z}\right] + \mu\left[\frac{\partial^2 \overline{w}}{\partial x^2} + \frac{\partial^2 \overline{w}}{\partial y^2} + \frac{\partial^2 \overline{w}}{\partial z^2}\right], \tag{1c}$$

where $\overline{u}$, $\overline{v}$, $\overline{w}$ are time-averaged velocity components, u', v', w' are the fluctuating velocity components, following the standard Reynolds decomposition. The momentum budgets on the right-hand side of these equations indicate that the mean pressure field is produced due to three different aspects: the first three terms belong to the velocity convection of the mean flow field; the three Reynolds stress terms in the middle are attributed to the fluctuating velocity field; the last three terms are generated due to the momentum diffusion by viscous effects.

It is noticed that, as a scalar field, the pressure field can be estimated with a single component of the three-dimensional pressure gradients, on the condition that the pressure boundary can be determined. For instance, in the turbulent wake investigated here, an integration path in the y direction [orange dashed line in Fig. 3(b)] can be chosen such that the pressure along the path is given by $\overline{p} = \int \frac{\partial \overline{p}}{\partial y} dy$. Since the pressure at $y \to \pm\infty$ is close to the ambient pressure ($p - p_\infty \approx 0$), it can be used as a boundary condition to perform pressure integration. Expanding this integration path to the whole three-dimensional domain, the scalar field of pressure can be estimated using a one-dimensional (1D) equation only.

For base-pressure analysis, an integration path close to the base (outside the boundary layer) can be chosen to approximate it [Fig. 3(b)]. The viscous diffusion terms are expected to concentrate in the region of significant shear, such as the boundary layer, the separation/reattachment positions, and the near-wall regions, while their contributions to the separated turbulent wake of high Re are relatively low. Therefore, for the separated turbulent wake, the viscous terms can be neglected, and the y component of the RANS equation becomes

$$\frac{\partial \overline{p}}{\partial y} = \underbrace{-\rho\left[\overline{u}\frac{\partial \overline{v}}{\partial x} + \overline{v}\frac{\partial \overline{v}}{\partial y} + \overline{w}\frac{\partial \overline{v}}{\partial z}\right]}_{A_M} \underbrace{-\rho\left[\frac{\partial \overline{u'v'}}{\partial x} + \frac{\partial \overline{v'v'}}{\partial y} + \frac{\partial \overline{v'w'}}{\partial z}\right]}_{A_F} = A_y. \tag{2}$$

It shows that the mean pressure force is compensating for inertial forces due to the acceleration of the mean flow A_M, and forces originating from the Reynolds stresses. As a reminder, it is also equal to the y component of the mean acceleration of the flow $A_y = A_M + A_F$, where A_F is the mean acceleration of the fluctuating field. According to the spatial gradient, these terms can be further noted as $A_{Mx}, A_{My}, A_{Mz}, A_{Fx}, A_{Fy}$, and A_{Fz}. For completeness, the viscous diffusion terms are marked as $A_V = A_{Vx} + A_{Vy} + A_{Vz}$. The global contribution of each component to the total pressure gradient is evaluated quantitatively by the volume (or surface for 2D cases) integration of its absolute value in the whole computational domain (or in a particular region of interest if needed), given by

$$\eta_n = \frac{\iiint |A_n| dV}{\sum_{i=1}^{9} \iiint |A_i| dV}, \tag{3}$$

where A_n or A_i is the nth or ith term on the right-hand side of Eq. 1(b), viscous terms included.

To assess the local pressure components generated by each term, Eq. (2) is integrated along the y direction with a zero-value boundary condition at the path end. The integrated pressure from $\partial \overline{p}/\partial y$ is given by

$$\begin{aligned} \overline{p} = \int \frac{\partial \overline{p}}{\partial y} dy = & \underbrace{-\int \rho \overline{u} \frac{\partial \overline{v}}{\partial x} dy}_{\overline{p_{Mx}}} \underbrace{- \int \rho \overline{v} \frac{\partial \overline{v}}{\partial y} dy}_{\overline{p_{My}}} \underbrace{- \int \rho \overline{w} \frac{\partial \overline{v}}{\partial z} dy}_{\overline{p_{Mz}}} \\ & \underbrace{-\int \rho \frac{\partial \overline{u'v'}}{\partial x} dy}_{\overline{p_{Fx}}} \underbrace{- \int \rho \frac{\partial \overline{v'v'}}{\partial y} dy}_{\overline{p_{Fy}}} \underbrace{- \int \rho \frac{\partial \overline{v'w'}}{\partial z} dy}_{\overline{p_{Fz}}}. \end{aligned} \tag{4}$$

It is noticed that, for incompressible flow, $\overline{p_{Fy}} = -\int \rho \frac{\partial \overline{v'v'}}{\partial y} dy = -\rho \overline{v'v'}$, which indicates that the Reynolds normal stress $\overline{v'v'}$ directly contributes to low pressure. It is worth distinguishing between the global integration Eq. (3) and the local integration Eq. (4) in momentum decomposition—the former is used to assess the global contribution of each momentum budget to the pressure gradient, while the latter is used to evaluate their pressure contributions at specific locations. For some momentum budgets, such as the Reynolds normal stress $\overline{v'v'}$, it produces a momentum budget A_{Fy} with positive and negative zones that appear in pairs in the field, which yields an infinitesimal value when performing global integration of the signed true value, significantly underestimating its pressure gradient contributions. Therefore, in the global integration, the absolute value is used in Eq. (3), while when assessing their local pressure contributions (4), the signed true value is used to reveal the physical compensation among competing mechanisms in the pressure balance. Finally, although the pressure decomposition method is proposed based on the y component, it equally applies to the other two components, depending on the configuration of the fluid system and the analyzing target.

A summary of the momentum budgets, their mathematical definition, physical effect, and typical manifestation is illustrated in Fig. 1, totaling five different mechanisms of pressure-field generation. In the framework of momentum decomposition, the contributions from these terms or physical effects can be rigorously distinguished and quantitatively evaluated according to their precise mathematical definition.

(1) *Mean flow terms A_{Mx} and A_{Mz} (streamline curvature effect).* These two terms correspond to the physical meaning of streamline curvature effect, and the difference between them is the plane of motion (e.g., A_{Mx} operates in the x-y plane). Taking A_{Mx} as an example, requires the coexistence of a streamwise velocity $\overline{u}$ and the streamwise gradient of the lateral velocity $\partial \overline{v}/\partial x$. These terms take effect when both components appear, which indicates that the streamwise streamline undergoes deflection in the cross-stream direction, in agreement with the well-established streamline curvature effect. A unique feature is that the previous interpretation of the streamline curvature effect relies heavily on empirical observation, while in the framework of momentum decomposition, their pressure contribution can be rigorously distinguished and exactly quantified.

(2) *Mean flow terms A_{My} (flow acceleration effect).* This term captures the pressure field induced by the convective acceleration of the mean flow. As its definition, it consists of the lateral velocity $\overline{v}$

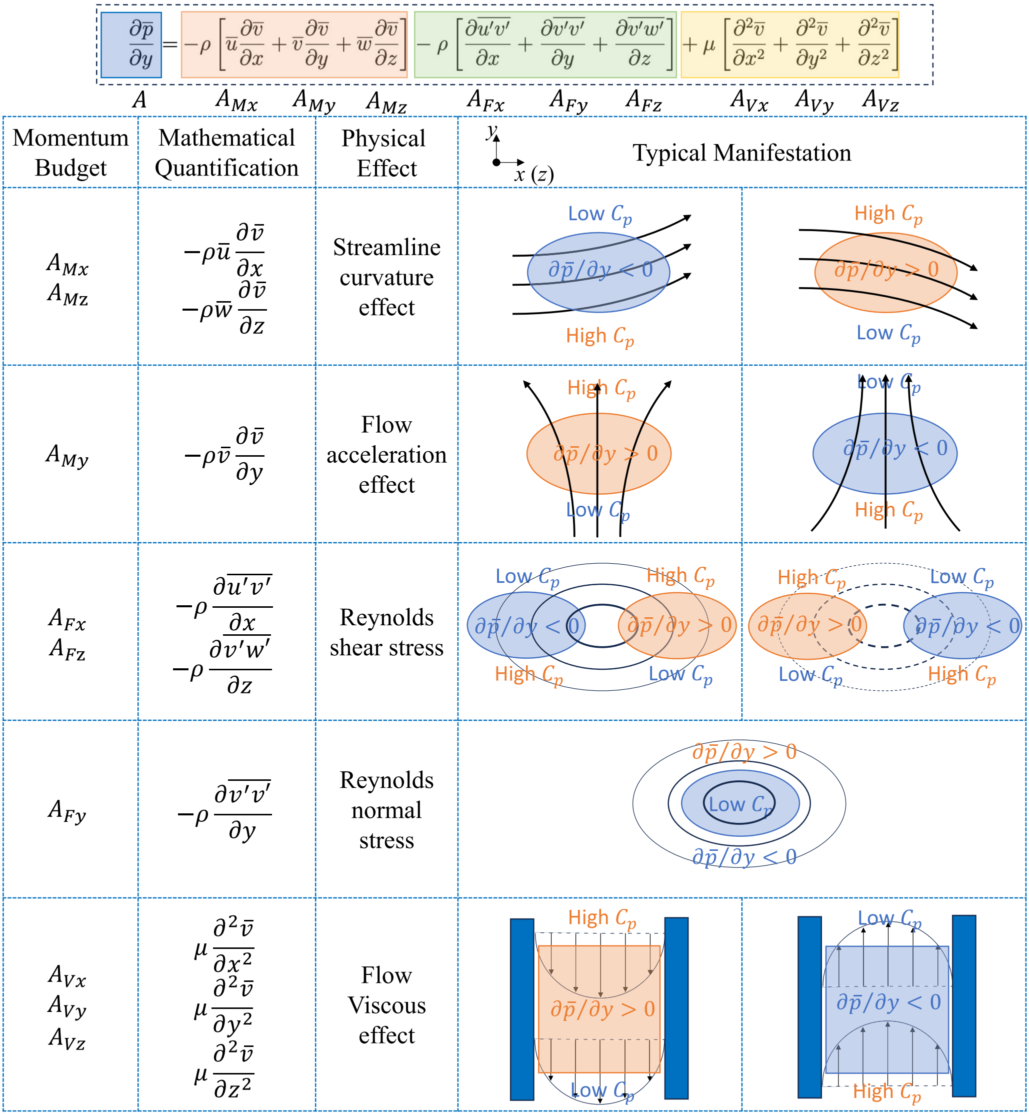

$$\underset{A}{\frac{\partial\bar{p}}{\partial y}} = -\rho\left[\underset{A_{Mx}}{\bar{u}\frac{\partial\bar{v}}{\partial x}} + \underset{A_{My}}{\bar{v}\frac{\partial\bar{v}}{\partial y}} + \underset{A_{Mz}}{\bar{w}\frac{\partial\bar{v}}{\partial z}}\right] - \rho\left[\underset{A_{Fx}}{\frac{\partial\overline{u'v'}}{\partial x}} + \underset{A_{Fy}}{\frac{\partial\overline{v'v'}}{\partial y}} + \underset{A_{Fz}}{\frac{\partial\overline{v'w'}}{\partial z}}\right] + \mu\left[\underset{A_{Vx}}{\frac{\partial^2\bar{v}}{\partial x^2}} + \underset{A_{Vy}}{\frac{\partial^2\bar{v}}{\partial y^2}} + \underset{A_{Vz}}{\frac{\partial^2\bar{v}}{\partial z^2}}\right]$$

Momentum Budget	Mathematical Quantification	Physical Effect	Typical Manifestation
A_{Mx} A_{Mz}	$-\rho\bar{u}\frac{\partial\bar{v}}{\partial x}$ $-\rho\bar{w}\frac{\partial\bar{v}}{\partial z}$	Streamline curvature effect	
A_{My}	$-\rho\bar{v}\frac{\partial\bar{v}}{\partial y}$	Flow acceleration effect	
A_{Fx} A_{Fz}	$-\rho\frac{\partial\overline{u'v'}}{\partial x}$ $-\rho\frac{\partial\overline{v'w'}}{\partial z}$	Reynolds shear stress	
A_{Fy}	$-\rho\frac{\partial\overline{v'v'}}{\partial y}$	Reynolds normal stress	
A_{Vx} A_{Vy} A_{Vz}	$\mu\frac{\partial^2\bar{v}}{\partial x^2}$ $\mu\frac{\partial^2\bar{v}}{\partial y^2}$ $\mu\frac{\partial^2\bar{v}}{\partial z^2}$	Flow Viscous effect	

FIG. 1. A schematic summary of the momentum budgets, their mathematical definition, physical effect, and typical manifestation. In A_M, the black solid curve with an arrow illustrates the streamline. In A_F, the black curves indicate the contour line of the Reynolds stresses ($\overline{u'v'}$ for A_{Fx}, $\overline{v'v'}$ for A_{Fy}, and $\overline{v'w'}$ for A_{Fz}) denoting their spatial distribution, with thickness showing their magnitude and solid curves for positive values and dashed ones for negative. In A_V, it is a simple demonstration by steady viscous pipe/duct flow with velocity profiles, while this term may also be significant in other high-shear regions, such as the boundary layer and the near-wall zones.

and its spatial acceleration in y direction. The integrated pressure from this term is given by $\overline{p_{My}} = -\int \rho\bar{v}\frac{\partial\bar{v}}{\partial y}dy = -\frac{1}{2}\rho\bar{v}^2$, which recovers the classic form associated with the Bernoulli principle. Indeed, for a steady, unidirectional, inviscid flow, the governing momentum decomposition Eq. (4) reduces to the Bernoulli equation, demonstrating that A_{My} rigorously quantifies this classic balance.

(3) *Fluctuating field terms* A_{Fx} *and* A_{Fz} *(Reynolds shear stress)*. These two terms quantify the contribution of the Reynolds shear stresses to the pressure field. For instance, near the upstream

side of the positive $\overline{u'v'}$ zone, there exists a positive streamwise gradient of $\overline{u'v'}$ ($\frac{\partial \overline{u'v'}}{\partial x} > 0$ there), corresponding to negative A_{Fx}. Through integration in the y direction, it produces a relatively low-pressure region near the upper side of the upstream and a relatively high-pressure region on the lower side. On the downstream side, its effect is reversed due to the different spatial pressure gradient it produces.

(4) *Fluctuating field terms A_{Fy} (Reynolds normal stress).* This term originates from the Reynolds normal stress $\overline{v'v'}$. The integrated pressure from this term is given by $\overline{p_{Fy}} = -\int \rho \frac{\partial \overline{v'v'}}{\partial y} dy = -\rho \overline{v'v'}$. Thus, the Reynolds normal stress directly contributes to a negative pressure proportional to its local strength, since the Reynolds normal stress is always positive if not zero.

(5) *Viscous diffusion term A_V (flow viscous effects).* This term illustrates the effect of flow viscosity on the pressure gradient. The most straightforward demonstration of this term is probably the simple steady duct flow or pipe flow, which does not contain pressure contributions from the other terms but only the viscous ones. It indicates the pressure gradient generated by the steady motion of the viscous wall-bounded flow. Additionally, this term may also be evident in flow regions of significant shear, such as the boundary layer and the near-wall regions.

In numerical simulations such as LES and detached eddy simulation (DES), due to the LES filtering and subgrid-scale (SGS) modeling, there exist SGS stresses contributing to the total stresses, particularly on coarse meshes, where the contributions from the modeled stresses are significant. In this sense, when the contributions from the SGS stresses are non-negligible, the fluctuating term A_F can be reformulated as follows to include the SGS stresses:

$$A_F = A_{Fx} + A_{Fy} + A_{Fz} = -\rho \frac{\partial(\overline{u'v'} + \overline{u'v'}_{SGS})}{\partial x} - \rho \frac{\partial(\overline{v'v'} + \overline{v'v'}_{SGS})}{\partial y} - \rho \frac{\partial(\overline{v'w'} + \overline{v'w'}_{SGS})}{\partial z}, \tag{5}$$

where $\overline{u'v'}_{SGS}$, $\overline{v'v'}_{SGS}$, and $\overline{v'w'}_{SGS}$ are SGS stresses.

The momentum decomposition framework provides a rigorous method for attributing pressure-field generation to distinct physical mechanisms. It enables both the quantitative evaluation of each mechanism's contribution and the spatial mapping of its distribution—crucial capabilities for flow diagnostics and control. As summarized in Fig. 1, the pressure field is decomposed into specific, quantifiable momentum budgets, each corresponding to a unique physical mechanism (e.g., streamline curvature, Reynolds stresses). This decoupling allows the complex contributions of turbulent flow to the pressure field to be disentangled and analyzed by mechanism. Consequently, interpreting the pressure field relies on understanding the balance and compensation among these competing physical mechanisms. Ultimately, this framework provides a foundational basis for developing and rationally analyzing flow control strategies, as the control mechanisms can be directly linked to the manipulation of specific momentum budgets.

Compared with the previous models [4–6], the current approach does not explicitly integrate the whole separation bubble. Instead, an integration path or surface close to the base is chosen to approximate the base pressure, analyzing the origin of base pressure and the mechanism of flow control. The base pressure seems dependent only on the local flow properties along this path, while the effect of the global wake shape on base pressure is accounted for implicitly by the feedback of the downstream flow on the upstream velocity field: as the global wake shape or separation streamline changes, the velocity field along the integration path changes with it. In turn, it is expected that effective flow control methods should eventually manipulate the flow along this region, either directly or indirectly. The decomposition method proposed here is based on the RANS equations, largely independent of flow conditions, making this method more universal and flexible.

To analyze the flow components contributing to the dynamic forces on an immersed body, force decomposition methods have been developed. In particular, the force partitioning method proposed by Zhang [42], Menon and Mittal [43] effectively decomposes the force components according to their force-producing mechanisms, which enhances our understanding of the generative mechanism of forces in complex flow systems such as flow-induced vibration. Combining the force partitioning method and modal decomposition techniques, model force partitioning is proposed by Prakhar *et al.* [44] to identify the key flow structures contributing to the time-varying aerodynamic loads. By comparison, the force partitioning method mainly focuses on partitioning the forces on the body and their dynamic evaluation, while the momentum decomposition is based on statistical flow quantities and decomposes the physical mechanisms contributing to the pressure field, which may also approximate the pressure distribution or force on the body. The force partitioning method gives the time series of body forces, which are spatially integrated, and the energy extraction method is employed to evaluate their contributions. Whereas the momentum decomposition reveals the spatial distributions of the momentum budgets, quantifying different physical mechanisms contributing to the pressure field, which can be directly evaluated by their pressure contributions, suitable for complex turbulent flow.

Finally, it is important to distinguish the momentum decomposition from the pressure Poisson equation. The Poisson equation allows direct calculation of the instantaneous pressure field, and the source terms on the right-hand side of the equation can be divided into contributions from rate-of-strain and vorticity [45]. Different from the coupled second-order derivatives in the Poisson equation, the momentum decomposition method directly resolves the pressure gradient into contributions from identifiable physical mechanisms and quantitatively evaluates each. Derived straightforwardly from the Reynolds-averaged momentum equations, this approach provides an intuitive, mechanism-based interpretation of pressure generation. This physical insight is essential for understanding the pressure generation mechanism and forms a rigorous foundation for designing and analyzing targeted flow control strategies.

III. DATABASE

Two datasets are analyzed in the present study, one belonging to a DNS of laminar flow around an elliptic cylinder at $\mathrm{Re}_D = 200$, the other one being a 3D LES of turbulent axisymmetric bluff body wake at $\mathrm{Re}_D = 1.88 \times 10^5$. The purpose of the numerical simulations is to provide a resolved dataset for performing the analysis, while the momentum decomposition equally applies to experimental data. The laminar cylinder flow serves as a demonstration of the momentum decomposition method, and the turbulent wake illustrates its application for analyzing complex turbulent flow and flow control.

In DNS, laminar flow past an elliptic cylinder with aspect ratio of $AR = L/D = 1.25/0.8$ (L and D are the length and width of the cylinder, respectively) is investigated with a computational domain of $L = 31.25D + 62.5D$, $W = 62.5D$, $H = 2.5D$, as illustrated in Fig. 2(a). The computational mesh is a hex-dominant mesh generated with snappyHexMesh. In the vicinity of the cylinder, the mesh is refined to resolve the key flow structures, keeping the maximum $y^+ < 7.33 \times 10^{-3}$, which results in a 2D mesh with 1.48×10^5 cells in total.

The DNS simulation is performed with the open-source package OpenFOAM, with an adjustable time step keeping the Courant number less than 0.8. The inlet flow is fixed as a uniform stream in the x direction, which gives a Reynolds number of $\mathrm{Re}_D = 200$, and a no-slip boundary is used for the cylinder body. Both the spatial and temporal terms of the compressible NS equations are discretized with second-order numerical schemes.

In LES, the three-dimensional turbulent wake [Figs. 3(c) and 3(d)] is generated by an axisymmetric bluff body with a blunt trailing edge at $\mathrm{Re}_D = 1.88 \times 10^5$ (the diameter of the body is $D = 0.1965$ m and the inlet velocity is $U_\infty = 15$ m/s). The LES is performed with a one-equation eddy-viscosity SGS model in a cylindrical computational domain with $5D$ diameter and $11D$ length, solving compressible NS equations with the Pimple algorithm. The numerical scheme is second-order since a preliminary study shows that a first- and second-order blended scheme may lead to damping of key flow dynamics. A fully structured mesh with 4.5 million hexahedral cells is used to resolve the turbulent wake, with refinement zones in the near wake region [Fig. 3(a)]. On average, the spatial resolution of the near wake region ($0 < x/D < 2$ and $r/D < 0.5$) is $\Delta x/D = 0.00916$.

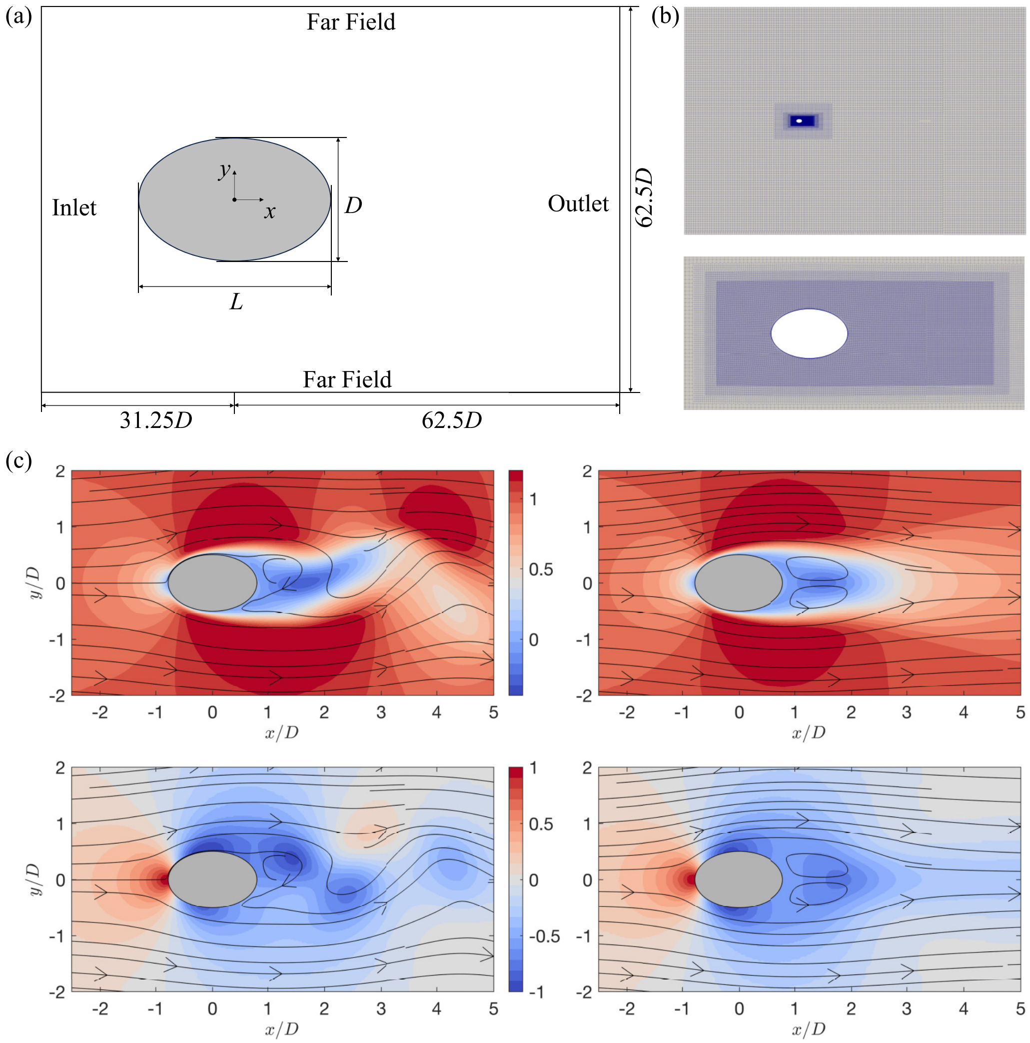

FIG. 2. (a) The computational domain and the model geometry, not to scale. (b) A slice of the computational mesh on the x-y plane, and the amplified views of the refined region. (c) The normalized streamwise velocity field (first row) and the pressure distribution (second row) for the instantaneous (left column) and time-averaged flow (right column).

On the inlet boundary near the wall, the inlet velocity is prescribed according to the law of the wall, given by

$$\begin{aligned} U &= U_\infty, & y^+ &> \delta^+ \\ U^+ &= \tfrac{1}{\kappa}\ln y^+ + C^+, & \delta^+ \geqslant y^+ &> y_i^+ \\ U^+ &= y^+, & y^+ &\leqslant y_i^+, \end{aligned} \tag{6}$$

where $y^+ = y\,U_\tau/\nu$, $U^+ = U/U_\tau$, $\delta^+ = \delta\,U_\tau/\nu$, δ is the thickness of the boundary layer, U_τ is the friction velocity, and $\kappa = 0.41$, $C^+ = 5$. A nonreflecting pressure boundary condition is used on the

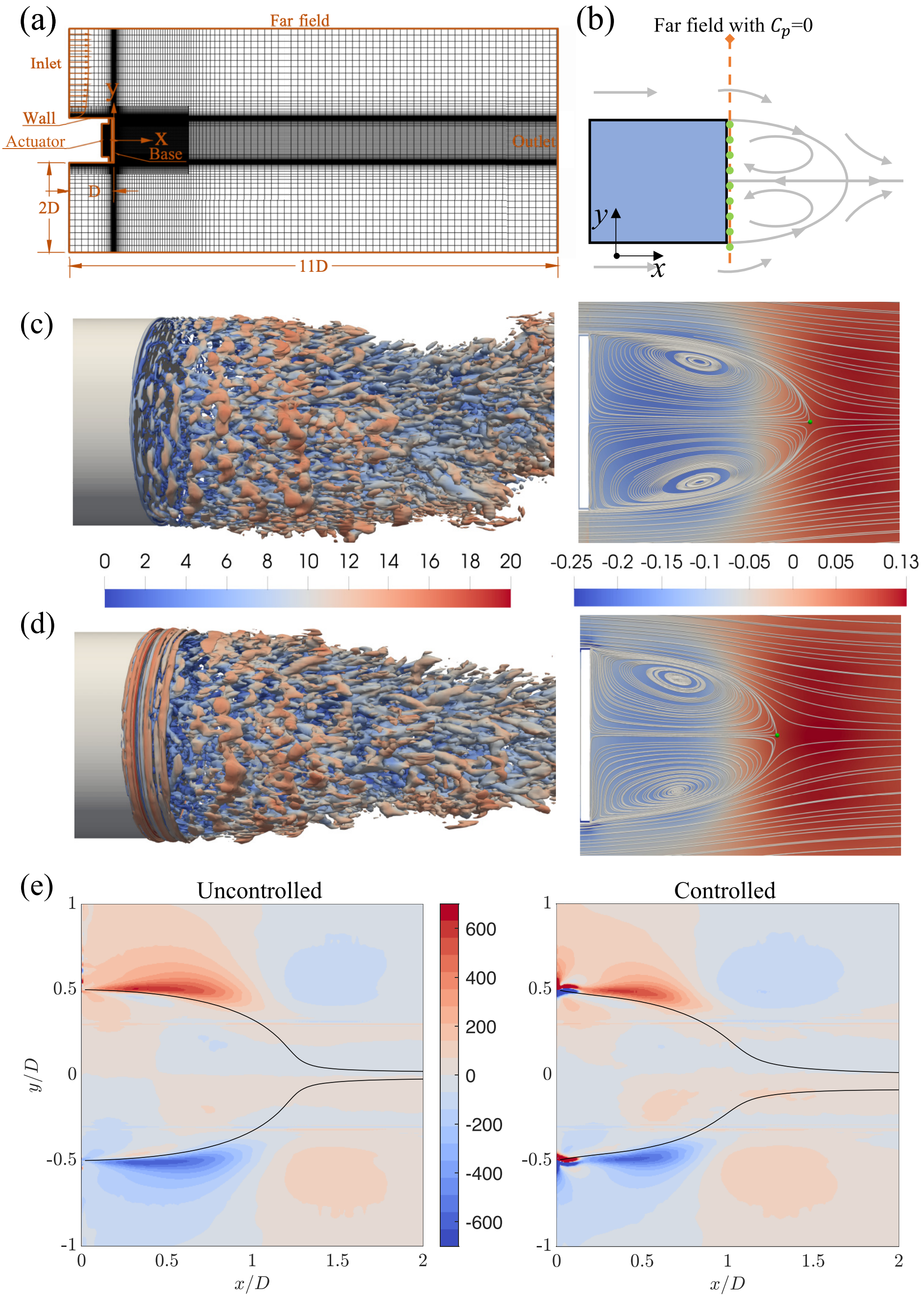

FIG. 3. (a) A slice of the computational mesh and the model geometry on the *x*-*y* plane. (b) A schematic of the time-averaged streamline distribution and the integration path. The instantaneous flow field identified by the Q criterion (colored by the velocity magnitude, $0 < U < 20$ m/s) and the time-averaged streamline and pressure field ($-0.25 < \overline{\langle C_p \rangle} < 0.13$) for (c) the uncontrolled wake and (d) the controlled wake. (e) The y component of the pressure gradient for the uncontrolled wake and the controlled wake. The units in the pressure gradient contour are Pa/m.

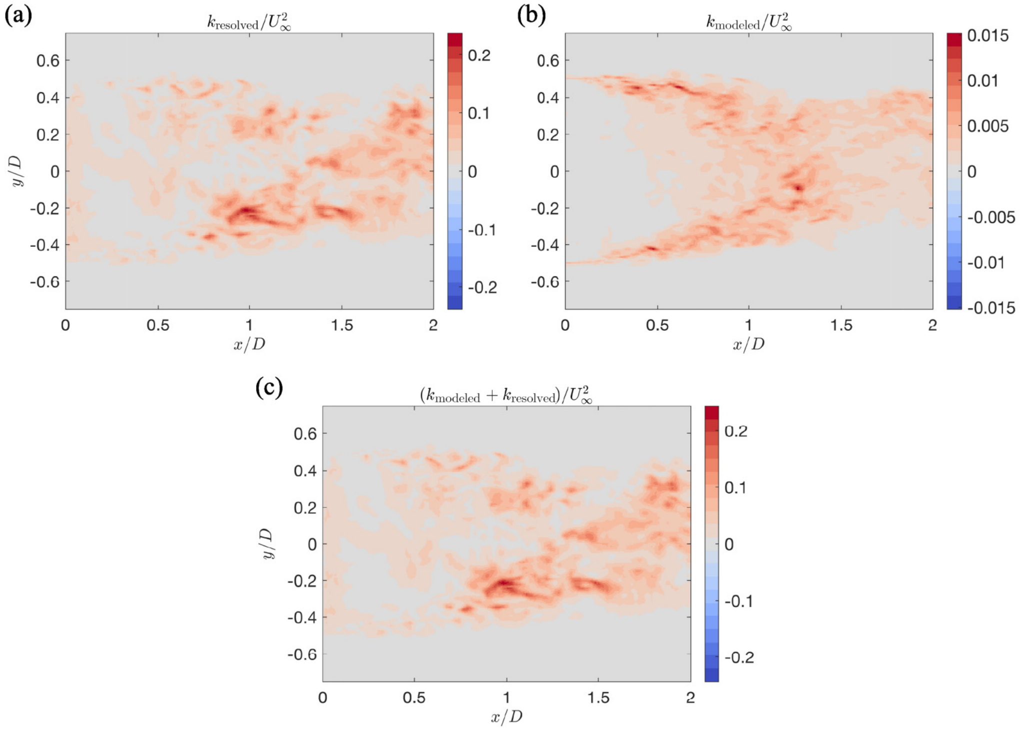

FIG. 4. A comparison of (a) the resolved TKE $k_{\text{resolved}}/U_\infty^2$(b) the modeled TKE $k_{\text{modeled}}/U_\infty^2$ and (c) their superposition $(k_{\text{resolved}} + k_{\text{modeled}})/U_\infty^2$ in the uncontrolled turbulent case.

boundary of the computational domain to prevent pressure reflection, determined by solving

$$\frac{\partial \phi}{\partial t} + (U_n + c)\frac{\partial \phi}{\partial n} = 0, \tag{7}$$

where ϕ is the flux field, n is the outward-pointing unit normal vector, c is the speed of sound, and U_n is the advection velocity parallel to the boundary normal direction. A no-slip velocity boundary condition is applied to the wall. To fully resolve the slow dynamics of the turbulent axisymmetric wake (such as the multistability), a very long nondimensional timescale of $TU_\infty/D = 5500$ is resolved. The pressure coefficient C_p is defined as $C_p = (p - p_\infty)/0.5\rho U_\infty$, where p_∞ is the reference pressure. The area-weighted averaged pressure coefficient on the base is marked as $\langle C_p \rangle$. The pulsed jet velocity is expressed as a blowing coefficient given by $C_\mu = u_f^2 A_j / U_\infty^2 A_b$, where u_f is the amplitude of the pulsed jet, A_j and A_b are the area of the jet boundary and the base, respectively. The frequency is expressed as the Strouhal number $St_D = fU_\infty/D$.

To evaluate the contribution of the SGS stresses to the total stresses, based on the instantaneous flow field available, the resolved turbulent kinematic energy [TKE, $k_{\text{resolved}} = 0.5(u'u' + v'v' + w'w')$] is compared with that modeled by the SGS (k_{modeled}). As shown in Fig. 4, the SGS modeled stresses mainly concentrate in the vicinity of the shear layer and the wake region where the shear layers merge (near $x/D = 1$), while the resolved TKE is distributed in the whole near wake region with peaks close to $x/D = 1$. By comparison, the maximum $k_{\text{resolved}}/U_\infty^2$ is 0.248, while the maximum $k_{\text{modeled}}/U_\infty^2$ is 0.015, only about 6% of that being resolved. A direct comparison of the resolved TKE k_{resolved} [Fig. 4(a)] with the total TKE [$k_{\text{modeled}} + k_{\text{resolved}}$, Fig. 4(c)] illustrates that adding the modeled TKE does not evidently change its distribution due to the low contribution from k_{modeled}. Therefore, in the current study, the turbulent flow structures are well resolved, and the

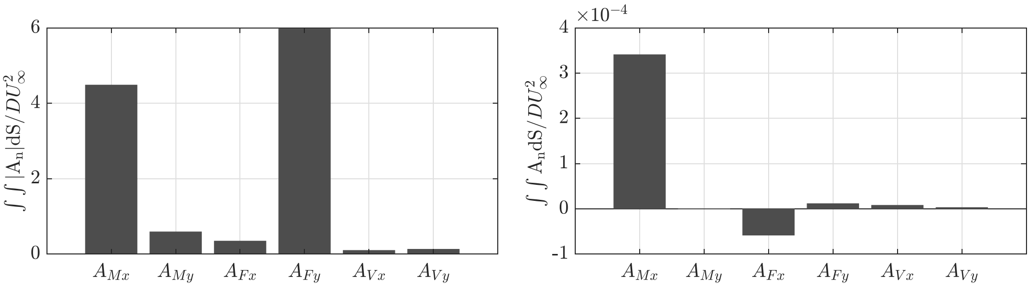

FIG. 5. The contribution of each momentum budget to the overall pressure gradient, evaluated with the absolute value (left figure, given by $\iint |A_n| \mathrm{dS}/DU_\infty^2$) and the signed true value (right figure, given by $\iint A_n \mathrm{dS}/DU_\infty^2$).

sensitivity of the total Reynolds stresses to the SGS modeling is low, indicating that it is sufficient to omit the SGS stresses and perform the analysis with the resolved flow structures.

In the controlled wake [Fig. 3(d)], for the purpose of pressure drag reduction, the separated shear layer near the base edge is manipulated with a high-frequency pulsed jet issued through a thin slot of 2 mm diameter underneath the base edge. The pulsed jet works at the frequency $f = 750$ Hz and velocity coefficient $C_\mu = 0.058$, corresponding to 20% base-pressure recovery. A more detailed numerical setup and an extensive validation of the numerical method and results, developed at Imperial College London, can be found in Zhu and Morrison [21] and Zhu *et al.* [46].

IV. DNS RESULTS AT $\mathrm{Re}_D = 200$

In the laminar regime of $\mathrm{Re}_D = 200$, the flow past the elliptic cylinder is unsteady with periodic shedding of alternative vortices, forming the Von Karman vortex street [Fig. 2(c)]. Near the body front, the inlet flow undergoes deceleration and stagnation, generating a high-pressure region. The large-scale flow separation in the rear produces low pressure on the base, contributing to the pressure drag. Although instantaneously the wake is symmetry-breaking due to the asymmetric vortex shedding, the mean flow field features a pair of symmetric recirculation bubbles after the time average of a nondimensional timescale $tU_\infty/D = 338.4$ due to the alternative sequence of vortex shedding from the opposite sides of the rear [Fig. 2(c)].

To quantitatively evaluate the global contribution of each momentum budget to the pressure gradient, surface integrations of each term over the computational domain are calculated, with a comparison of absolute value and signed true value (Fig. 5). The absolute value integration effectively detects the overall contribution of each momentum budget, with dominant contributions from the streamwise mean velocity term A_{Mx} and the Reynolds normal stress A_{Fy}. Although relatively low, the pressure field also receives contributions from the minor terms A_{My} and A_{Fx}, while the contribution from the viscous diffusion terms is very low, if not negligible. By comparison, the integration of the signed true value is extremely small (on the order of $\approx 10^{-4}$) due to the cancellations of positive gradients with the negative ones. Specifically, the contribution from the Reynolds normal stress A_{Fy} is seriously underestimated, with an integrated value close to zero. As defined, A_n refers to the nth momentum budget contributing to the pressure gradient instead of the pressure value itself. Therefore, for some momentum budgets, such as A_{Fy} from the Reynolds normal stress $\overline{v'v'}$, their positive and negative zones almost always appear in pairs, which always yields an infinitesimal value close to zero when performing global integration of the signed true value. Therefore, for a fair evaluation of the global pressure gradient contribution from each momentum budget, it is suggested to use the absolute value to perform global integration.

As illustrated in Fig. 6, the spatial distribution of each momentum budget indicates that the mean velocity term A_M mainly concentrates near the body front and outside the recirculation bubble, while

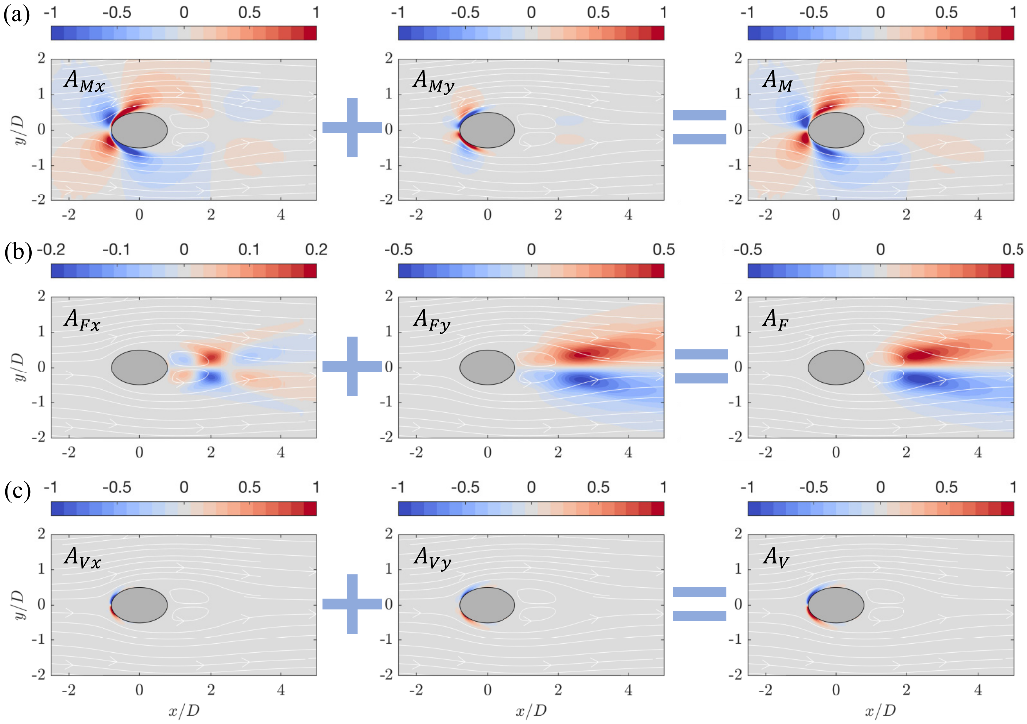

FIG. 6. The distribution of the momentum budgets contributing to pressure gradient, including (a) A_{Mx}, A_{My}, $A_M = A_{Mx} + A_{My}$, (b) A_{Fx}, A_{Fy}, $A_F = A_{Fx} + A_{Fy}$, (c) A_{Vx}, A_{Vy}, $A_V = A_{Vx} + A_{Vy}$, overlapped with the time-averaged streamline (white curves). All the budget terms are normalized with D/U_∞^2.

inside the recirculation bubble and downstream, the pressure gradient receives main contributions from the fluctuating field term A_F. In agreement with the low contribution of the viscous diffusion term A_V, it is only observed in the boundary layer of significant shear, mainly near the body front [Fig. 6(c)].

Figure 6(a) indicates that the high-pressure region near the body front and the low-pressure region near the two sides of the body are mainly produced by A_M. Slightly downstream, A_M generates a low-pressure region in the recirculation bubbles due to the pressure drop from outside the near wake. Further downstream, after the wake stagnation point $x/D = 0.2$, A_M contributes high pressure near the central line. Figure 6(b) illustrates that the fluctuating term A_F concentrates in the wake region where the flow is highly unsteady, producing low pressure near the wake, especially in the vicinity of the wake stagnation point.

Two characteristic positions are selected to perform pressure integration of the momentum budgets to understand the generative mechanism of the pressure field, one located in the near wake at $x/D = 1$, and the other one being the far wake after the wake stagnation point at $x/D = 2.5$, as illustrated in Fig. 7. Although both regions feature low pressure near the center, their generative mechanism are different. In the near wake, the bulk of low pressure is from the mean velocity term A_{Mx}, which manifests as a streamline curvature effect producing a pressure drop from outside the recirculation bubbles. Whereas, the pressure variation in the near wake is mainly from the Reynolds stresses, with the Reynolds shear stress term A_{Fx} contributing to evident pressure recovery. In the far wake, although the mean velocity term A_{Mx} produces positive pressure due to its favorable streamline curvature, the significantly low pressure from the Reynolds stresses compensates this high pressure, resulting in a low-pressure region in this area. Specifically, the bulk of low pressure is produced by the Reynolds normal stress A_{Fy}, contributing $\overline{C_{pFy}} = -0.46$ near the center, compared

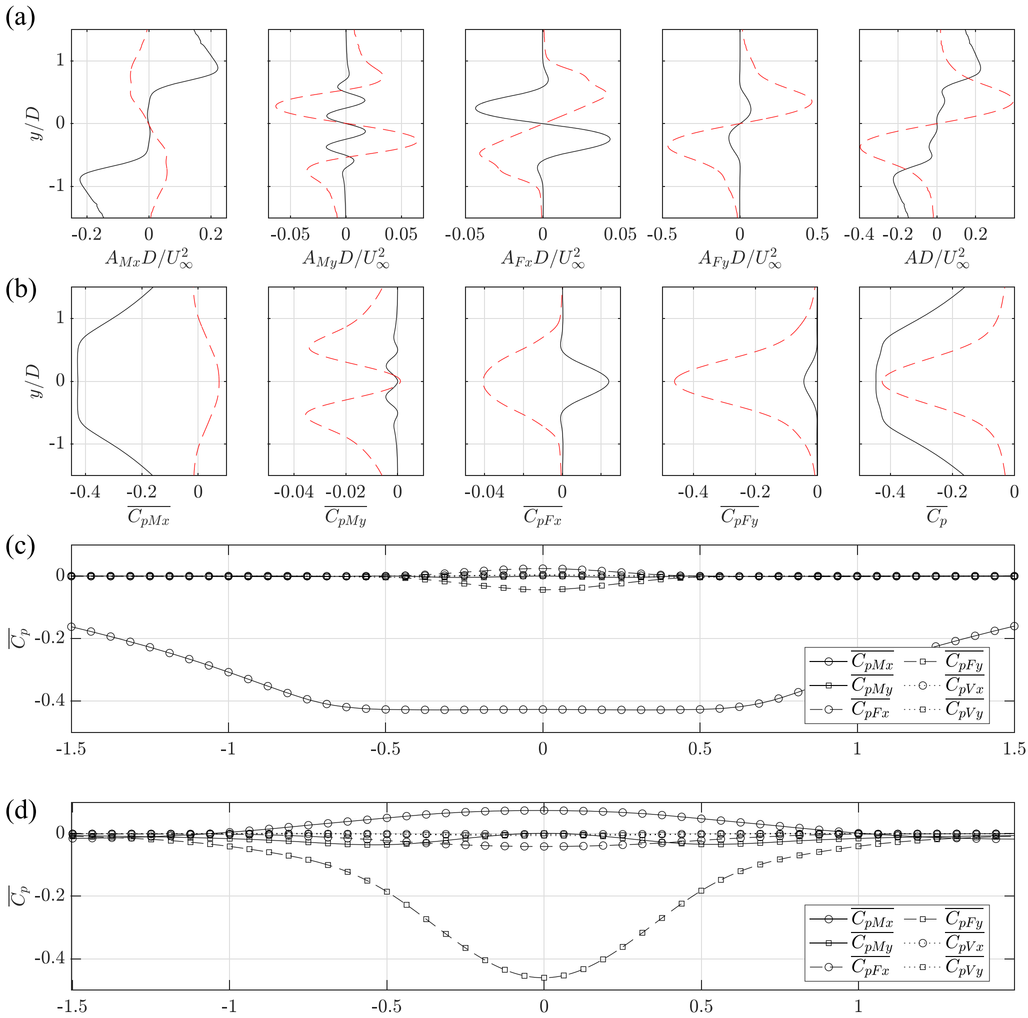

FIG. 7. (a) The distribution of each momentum budget at $x/D = 1$ (black solid curve) and $x/D = 2.5$ (red dashed curve), and (b) their integrated pressure. A comparison of the pressure contribution from each momentum budget for (c) $x/D = 1$ and (d) $x/D = 2.5$.

with $\overline{C_{pMx}} = 0.07$ from A_{Mx}. As expected, the pressure contribution from the viscous diffusion terms is negligible in this region.

It is worth noting that, compared with the turbulent flow of high Re, the pressure distribution near the wake stagnation point in the laminar flow is completely different. In the turbulent flow [Fig. 3(c)], there exists a high-pressure region of positive $\overline{C_p}$, while in the laminar state [Fig. 2(c)], a low pressure is observed in this region. As analyzed above, the low pressure in the laminar case is caused by the significant Reynolds stresses, which highlights the advantage of the momentum decomposition in understanding the generative mechanism of the pressure field.

V. LES RESULTS AT $\mathrm{Re}_D \approx 2 \times 10^5$

Although a detailed description of the LES results has been provided previously [21], it is discussed briefly here for completeness. The instantaneous uncontrolled turbulent wake [Fig. 3(c)] is a massively separated turbulent flow with a wide range of vortices of different sizes and forms. The sharp trailing edge causes flow separation and generates convective vortices parallel to the base edge. Downstream, these turbulence structures develop into some quasistreamwise braids which resemble the streamwise vortices in the turbulent mixing layer observed by Davoust *et al.* [47]. The time-averaged pressure field illustrates low-pressure regions near the recirculation bubbles and in the shear layer. Further downstream, a high-pressure region is generated close to the stagnation point. In the controlled case, a series of concentric vortex rings is generated in the vicinity of the base edge. By comparison, it illustrates that the control method reshapes the wake streamline and achieves a global pressure recovery in the whole wake, except for the base edge. It shows that the pressure rise in the controlled wake is accompanied by the reshaping of the wake, with the wake width narrowed and the separation streamlines becoming concave [21].

The distinction between the pressure fields generated by the controlled and uncontrolled turbulent wake can be illustrated by the lateral pressure gradient $\partial\overline{p}/\partial y$ [Fig. 3(e)]. Consistent with the pressure field, the uncontrolled pressure gradient shows a pair of large-scale gradient zones outside the separation streamline in the near wake (between $x/D = 0$ and $x/D = 1$), leading to low-pressure regions near the recirculation bubbles. Downstream, the favorable pressure gradient between $x/D = 1$ and $x/D = 2$ indicates a high-pressure region near the stagnation point. In the controlled wake, the pulsed jet produces significant pressure gradients in the vicinity of the separation point ($x/D = 0$, $y/D = \pm0.5$). In the outer region ($|y/D| > 0.5$), the pressure drop toward the wake produces low-pressure regions near the pulsed jet location. However, on the inner side, a pair of high-pressure gradient zones leading to a rapid pressure rise is generated, which is key for the base-pressure recovery.

A. Pressure-field decomposition

Although a qualitative description of the pressure distribution can be made by investigating the time-averaged velocity and the pressure fields (Fig. 3), the generative mechanism of such a distribution is not clear. By performing the momentum decomposition of the mean pressure field, the contribution of each momentum budget can be assessed, as shown in Fig. 8. In the complex multistable turbulent wake investigated here, whether controlled or not, only two budget terms contribute significantly to the pressure field, one belonging to the mean flow term $A_{Mx} = \overline{u}\partial\overline{v}/\partial x$ and the other one being the fluctuating field term $A_{Fy} = \partial\overline{v'v'}/\partial y$ (Fig. 8). In the uncontrolled wake, A_{Mx} and A_{Fy} take up 63.8% and 22.3%, respectively, totalling 86.1%. Similarly, in the controlled wake, these two terms contribute 61.1% and 20.8% (81.9% in total). As expected, the contribution of the viscous terms A_V is negligible in both cases, the sum of them being less than 0.1%.

It is noticeable that the three-dimensional terms (perpendicular to the x-y plane) A_{Mz} and A_{Fz} take up 7.6% in the uncontrolled wake and 8.6% in the controlled one, indicating that a 2D measurement of the wake could achieve reasonably accurate results. This is especially useful for experimental studies where 3D volumetric measurement is not feasible due to the huge cost.

Depending on their respective contributions, these momentum budgets can be classified into three categories: the major terms include A_{Mx} and A_{Fy}, as the main contributor to the pressure gradient ($\approx$80% in total); the minor terms (A_{My}, A_{Mz}, A_{Fx}, A_{Fz}) are relatively low compared with the major ones, each one taking up $\approx$ 5% or lower; due to the negligible contributions (<0.1%) from the viscous diffusion terms, they are classified into negligible terms, which are not further analyzed in the present work. Among the major terms, there exists a dominating one A_{Mx}, contributing over 60% of the pressure gradient.

Three-dimensional visualization of the major budget terms (A_{Mx} and A_{Fy}) is illustrated in Fig. 9 for the uncontrolled and the controlled wake. Both the mean flow term A_{Mx} and the fluctuating field term A_{Fy}, whether controlled or not, concentrate outside the separation streamline, which indicates that most pressure gradient originates from outside the wake. The positive or negative pressure gradients toward the wake are marked as A^+ and A^-, respectively, as shown in Fig. 9. It should be

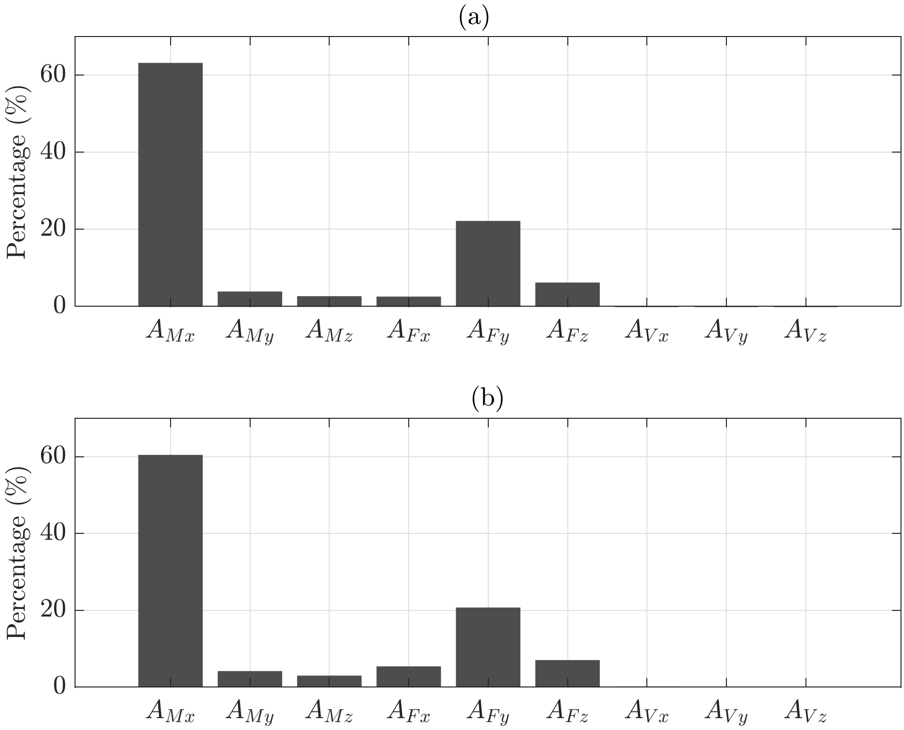

FIG. 8. The relative contribution of each momentum budget to the overall pressure gradient calculated with equation (3) for (a) the uncontrolled wake and (b) the controlled one.

noted that on the upper side of the wake ($y > 0$), the negative acceleration term ($A_i < 0$) indicates a positive pressure gradient toward the wake (A^+).

In the uncontrolled wake, the effect of A_{Mx} can be split into two regimes. Upstream, it produces a pair of large-scale negative pressure gradients toward the wake [A^- in Fig. 9(a)], resulting in low pressure in the recirculation bubble. Downstream, close to the stagnation point, the positive pressure gradient it generated indicates a high-pressure region near this location [A^+ in Fig. 9(a)], consistent with the pressure-field distribution in Fig. 3. The distinction between the uncontrolled wake and the controlled one is in the vicinity of the base edge. In the controlled wake, although A^- is generated near the outside of the base edge, on the inner side, the pulsed jet produces A^+, leading to a pressure rise toward the wake, which is key for base-pressure recovery. It is also noticed that the size of A^- is reduced near the recirculation bubble, and A^+ is enlarged, leading to higher pressure in the wake.

As expected, in both uncontrolled and controlled cases, A_{Fy} produces negative pressure gradients [A^- in Fig. 9(c)] both upstream and downstream of the wake, corresponding to the low pressure generated directly by the Reynolds normal stress $\overline{v'v'}$. In the controlled wake, the size of A_{Fy} is reduced, probably leading to slightly higher pressure as compared with the uncontrolled one.

Although contributing less than 20% in total, for completeness, the minor terms (Fig. 10) are also visualized to analyze their three-dimensional structures. The second mean flow term A_{My} consists of a pair of negative pressure gradient zones outside the wake and a large region of positive pressure gradient near the separation streamline, indicating a low-pressure region outside the separation streamline. It is noticed that, although the general topology of these structures is conserved in the controlled wake, a reduction in the A^- size and enlargement of A^+ is indicative of pressure recovery. A_{Mz} consists of four bubbles downstream outside the wake, contributing to negative pressure gradients. In the controlled wake, a region of a positive pressure gradient is generated near the base, as indicated by A^+ there, associated with the pressure recovery.

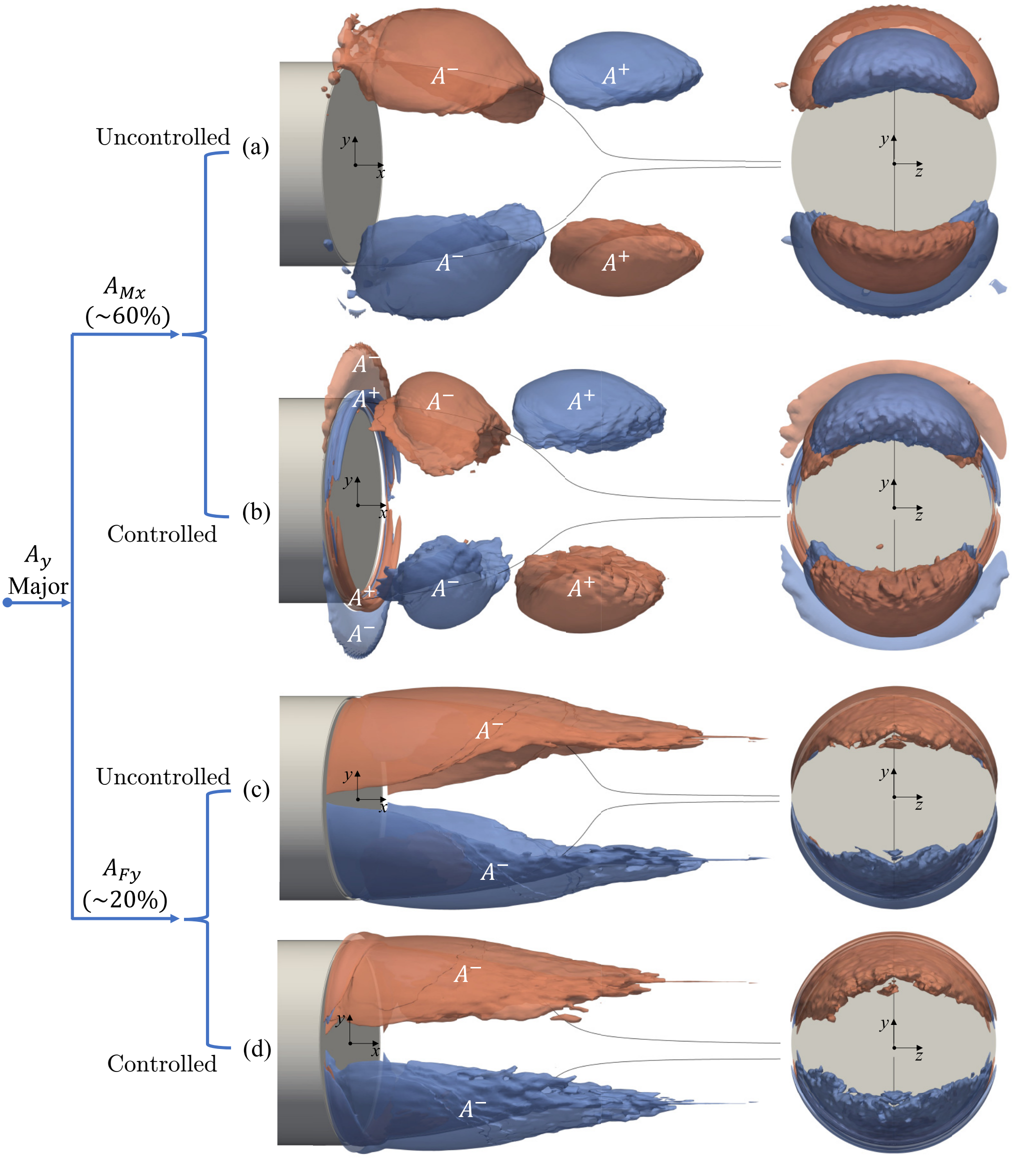

FIG. 9. Three-dimensional distribution of the major momentum budgets identified by $A_nD/U_\infty^2 = 0.11$ (red) and $A_nD/U_\infty^2 = -0.11$ (blue). A_{Mx} for (a) the uncontrolled wake and (b) the controlled wake, and A_{Fy} for (c) the uncontrolled wake and (d) the controlled wake. The left and right columns show side views perpendicular to the x-y and the y-z planes, respectively. The black curve marks the separation streamline originating from $y/D = \pm 0.5, x/D = 0, z/D = 0$. The white A^+ and A^- indicate pressure rise and drop toward the wake, respectively.

Contrary to the other three minor terms, A_{Fx} is located inside the wake, representative of the pressure gradient generated by the Reynolds shear stress. Noticeably, although this term produces large regions of A^- in the wake, A^+ is generated near the base, indicating that, despite introducing low pressure in the wake, it provides a favorable effect of increasing the base pressure. In the controlled case, an enlargement of the negative pressure gradient zone is observed, with an unfavorable effect

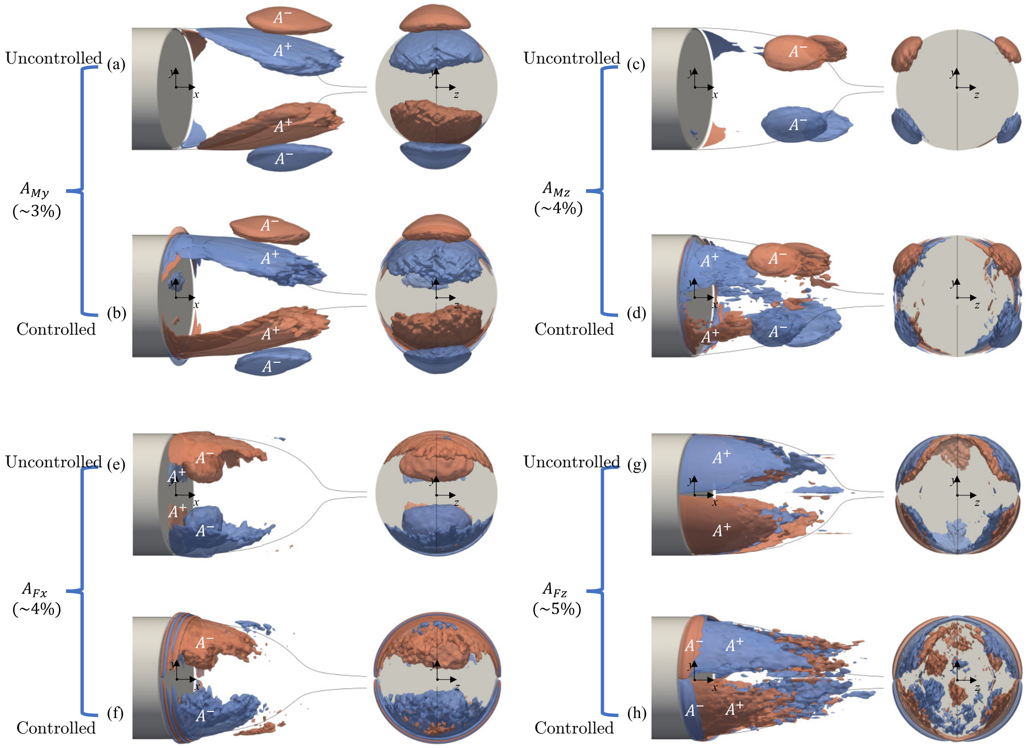

FIG. 10. Three-dimensional distribution of the minor momentum budgets identified by $A_nD/U_\infty^2 = 0.035$ (red) or $A_nD/U_\infty^2 = -0.035$ (blue). A_{My} for (a) the uncontrolled wake and (b) the controlled wake, A_{Mz} for (c) the uncontrolled wake and (d) the controlled wake, A_{Fx} for (e) the uncontrolled wake and (f) the controlled wake, and A_{Fz} for (g) the uncontrolled wake and (h) the controlled wake. The left and right columns in each subfigure show side views perpendicular to the x-y and the y-z planes, respectively. The black curve marks the separation streamline originating from $y/D = \pm 0.5$, $x/D = 0$, $z/D = 0$. The white A^+ and A^- indicate pressure rise and drop toward the wake, respectively.

of lower pressure from this term. A_{Fz} consists of four pairs of opposite pressure gradients slightly downstream of the base edge, illustrating low pressure along the shear layer.

B. Base-pressure decomposition

The base pressure is the force directly exerted on the bluff body, contributing to pressure drag, which is a core target for flow control. Therefore, in this section, the contribution of the momentum budgets to base pressure is analyzed by investigating the pressure gradient distribution close to the base (on the y-z plane at $x/D = 0.025$). This position is chosen outside the boundary layer to remove the viscous diffusion terms and unphysical gradient next to the base; the pressure at $x/D = 0.025$ closely resembles the base pressure at $x/D = 0$, with an average difference of $\Delta\overline{C_p} = 0.0066$.

As expected, the pressure distribution [Fig. 11(a)] illustrates that in the uncontrolled wake, there exists an evident pressure drop from the far field ($\overline{C_p} = 0$) to the base edge [marked by the dashed circle in Fig. 11(a)] where the time-averaged pressure coefficient is $\overline{C_p} \approx -0.1$. From the base edge to the base center, the pressure coefficient further decreases, producing a low-pressure region there. In the controlled wake, the pressure drop outside the base is enhanced, resulting in very-low-pressure regions near the outside of the base edge with a low peak value $\overline{C_p} < -0.2$. However, from the base edge toward the center, the pressure field rapidly recovers, producing high-pressure regions on the

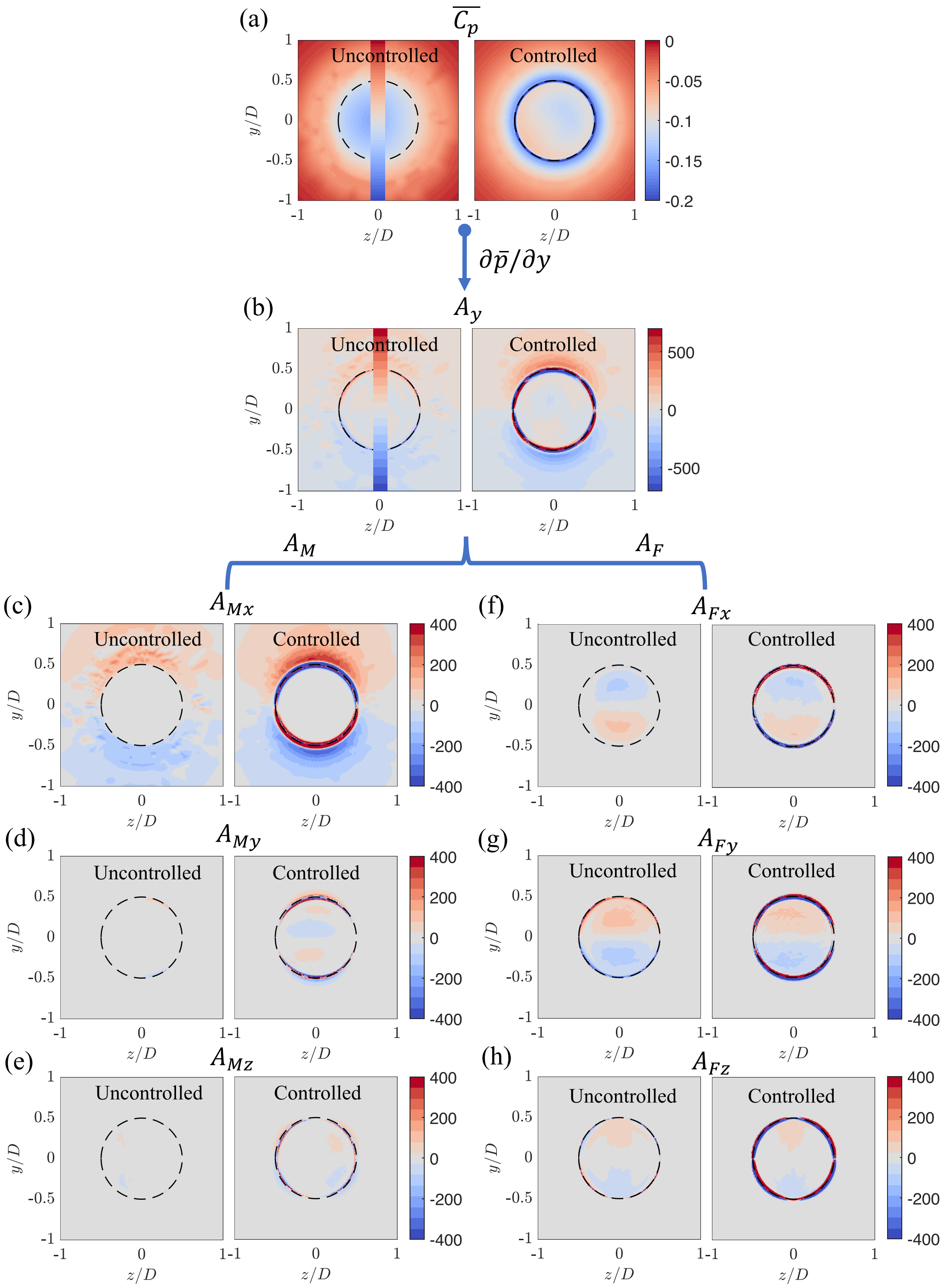

FIG. 11. The distribution of the pressure field, the pressure gradient, and the momentum budget terms close to the base (y-z plane at $x/D = 0.025$). (a) The time-averaged pressure field $\overline{C_p}$. (b) The y component pressure gradient $\partial\overline{p}/\partial y$. The acceleration terms contributing to the pressure gradient, including (c) A_{Mx}, (d) A_{My}, (e) A_{Mz}, (f) A_{Fx}, (g) A_{Fy}, and (h) A_{Fz}. In each subfigure, the left column shows the uncontrolled wake and the right column shows the controlled one. The units of the pressure gradient contour are Pa/m.

base [Fig. 11(a)]. Consistent with the pressure distribution, the pressure gradients [Fig. 11(b)] are indicative of pressure drop outside the wake in both controlled and uncontrolled wakes, while in the controlled case, there exists key pressure recovery near the inner side of the base edge.

In the uncontrolled wake, the budget terms [Figs. 11(c)–11(h)] illustrate that outside the wake, the pressure is generated by the mean flow term A_{Mx}, while inside the wake, the pressure contribution is mainly produced by the Reynolds stresses A_F. The distribution of the mean flow term A_{Mx} [Fig. 11(c)] agrees with the outside of A_y [Fig. 11(b)]. Among the fluctuating terms, A_{Fx} (produced by $\partial\overline{u'v'}/\partial x$) generates a positive pressure gradient on the lower side of the base and a negative pressure gradient on the upper, indicating that its effect is to increase the base pressure. The other two components of the fluctuating field terms A_{Fy} and A_{Fz} both produce low pressure on the base, indicative of pressure drag caused by the Reynolds normal stress $\overline{v'v'}$ and the Reynolds shear stress $\overline{v'w'}$.

With pulsed jet forcing, although the general topology of the momentum budget terms resembles those in the uncontrolled wake, significant pressure gradients are produced in the vicinity of the base edge [Figs. 11(c)–11(h)]. In A_{Mx}, the positive pressure gradient on the inner side of the base edge shows pressure rising toward the wake. Whereas, for the fluctuating terms A_F, the pressure gradients are more complex due to the high Reynolds stresses the pulsed jet produced there. In A_{Fx}, the negative pressure gradient near the base edge seems to cause an unfavorable pressure drop. The alternative pressure gradients across the base edge produced by A_{Fy} need a quantitative examination to evaluate their effect on base pressure. Finally, the negative gradient in A_{Fz} is shrunk, and positive gradients are produced near the base edge, indicative of pressure recovery.

C. Mechanism of flow control

To provide a quantitative evaluation of the base-pressure contribution and the effect of flow control, the pressure gradients produced by each momentum budget are taken from the middle section of the y-z plane at $z/D = 0$ in Fig. 11, and integrated to achieve the pressure components it produced, as illustrated in Fig. 12.

We first focus on the uncontrolled wake. The pressure gradients (2) and the integrated pressure components (4), together with the results taken directly from LES, are plotted in Fig. 12. Figure 12(a) shows that the calculated result agrees well with the LES result, which indicates that the proposed method based on the selected integration path is accurate. In $0.5 < |y/D| < 1$, numerical oscillation occurs due to mesh element change and the central differencing numerical scheme. The integration path crosses two regions of very different physical properties (Fig. 3): (i) the outer flow region lying outside the recirculating bubble ($|y/D| > 0.5$), where the flow is largely potential, and (ii) the inner flow region inside the recirculating bubble, where $|y/D| < 0.5$.

The bulk of low pressure is generated in the outer flow region outside the wake [Fig. 12(a)]. From the far field ($y/D = 2.5$) to the base edge ($y/D = 0.5$), the $\overline{C_p}$ drops from 0 to -0.113, indicating that the low pressure is already generated before reaching the wake. Compared with the lowest $\overline{C_p} = -0.158$ at $y/D = 0$, the pressure from the outer flow region takes up 71.5%. Therefore, the bulk of low pressure near the base originates from the region immediately outside the wake. Figure 12(a) shows that the peaks of the pressure gradient concentrate in the vicinity of the separation point ($y/D = \pm 0.5$), and the base pressure rapidly drops there. Thus, flow control targeting this region is expected to be effective for base-pressure manipulation.

As illustrated in Figs. 12(b)–12(g), there is no Reynolds stress contribution in the outer flow region that is thus steady, and only the first term $\overline{u}\partial\overline{v}/\partial x$ in Fig. 12(b) generates significant pressure variation. The change of curvature of the pressure profile at $|y/D| \approx 0.5$ in Fig. 12(b) marks the passage from the outer to the inner flow region. Since the mean streamwise velocity becomes close to zero and consequently its contribution to the pressure gradient too, as shown in Fig. 12(b), $\overline{C_{pMx}}$ remains constant but still dominates the other five pressure contributions in Figs. 12(c)–12(g) in the whole inner flow region. Although the pressure gradient from the second term ($\overline{u}\partial\overline{v}/\partial y$) is present in Fig. 12(c), its integration shows that its contribution to the overall base pressure

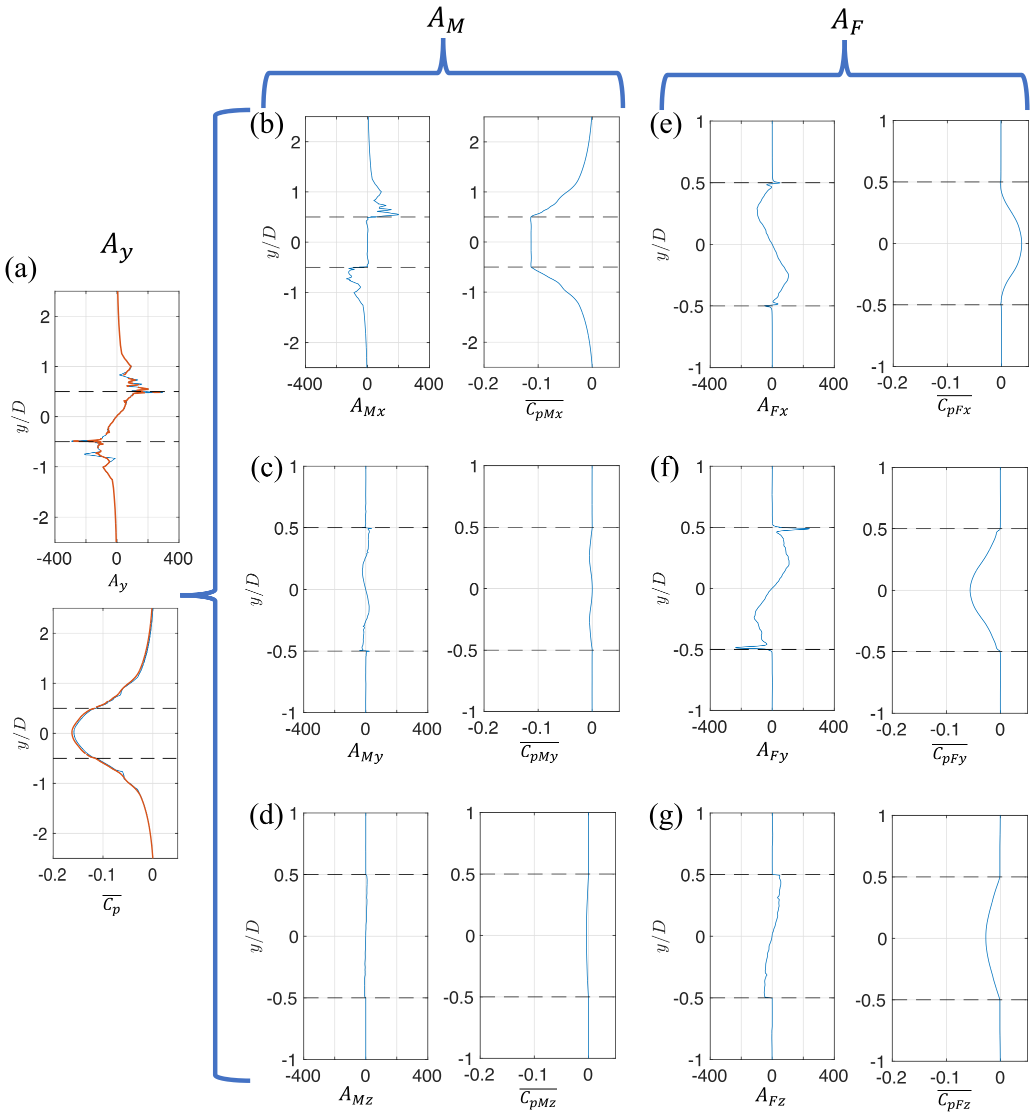

FIG. 12. The distribution of the pressure gradient and integrated pressure from each momentum budget along the integration path ($x/D = 0.025$). The base edge ($y/D = \pm 0.5$) is marked by the black dashed lines. In panel (a), the blue curve is from 3D LES, and the red dashed one is calculated from Eqs. (2) and (4). The units of the pressure gradient are Pa/m.

is negligible. In the case of an axisymmetric bluff body wake, although the instantaneous wake exhibits stochastic symmetry-breaking meandering, the long-time-averaged wake is axisymmetric. Therefore, the pressure from the third term ($\overline{w}\partial\overline{v}/\partial z$) is negligible since $\overline{w} \rightarrow 0$ [Fig. 12(d)].

In the inner flow region, the Reynolds stress terms in Figs. 12(e)–12(g) dramatically increase due to the turbulent motion. Their contributions to the base-pressure variation appear much larger than that of the mean recirculating flow, of which the main contribution is the lateral flow acceleration $\overline{u}\partial\overline{v}/\partial y$ shown in Fig. 12(c). Despite this mean-flow contribution, the pressure gradient in the inner flow region is essentially produced by the Reynolds stress gradients.

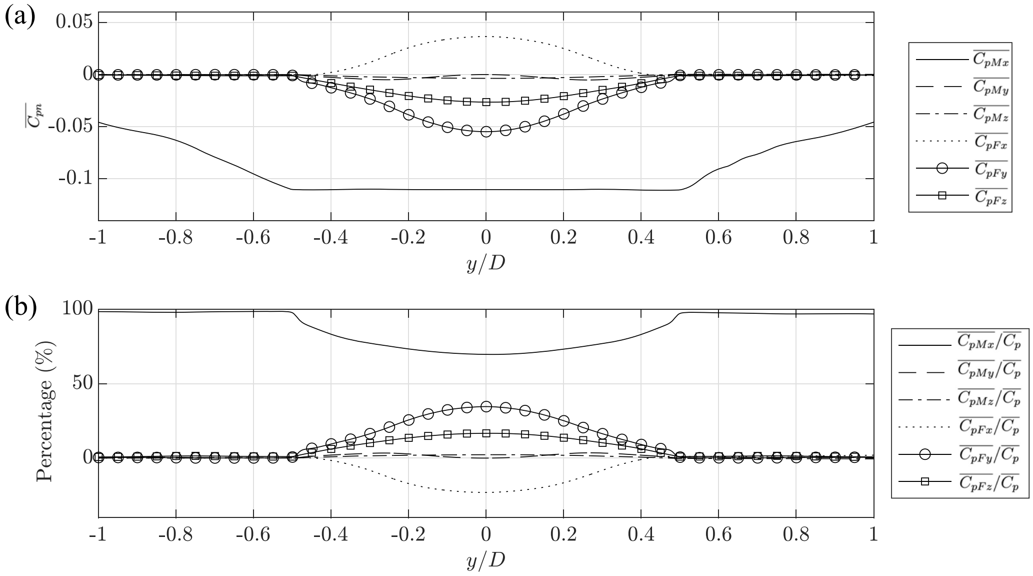

FIG. 13. (a) A comparison of the pressure contribution from each momentum budget, and (b) the relative contribution of them to the overall pressure at $x/D = 0.025$.

Of the three Reynolds stress gradient terms, A_F in Eq. (2), the first one in Fig. 12(e) is associated with a curvature effect in the x-y plane of the fluctuating flow in the inner flow region. However, it is the only component that increases the base pressure, likely due to opposite curvatures in the inner flow region. The second term A_{Fy} in Fig. 12(f) is directly generated by the lateral acceleration of the lateral component of the fluctuating field. It is compatible with a flow along the wall that alternates with time between two opposite directions: the first accelerating toward the center of the base and the second decelerating from the center of the base to the separation point. Finally, the last term in Fig. 12(g) is generated by the unsteady motion perpendicular to the x-y plane, linked to the effect of three-dimensional wake dynamics on base pressure.

Figure 13 shows a comparison of the integrated pressure from each acceleration term and their respective percentage contribution along the integration path. Clearly, the pressure from the first term $\overline{u}\partial\overline{v}/\partial x$ dominates the overall pressure. In the outer flow region, the first term takes up about 98% of the overall pressure, and in the inner flow region, its contribution is also higher than 70%. Other terms are evident only inside the inner flow region. Specifically, the second and the third terms are negligible; thus, only four terms are important: one mean velocity term $\overline{u}\partial\overline{v}/\partial x$ and three Reynolds stress gradients.

A comparison of the pressure components from the uncontrolled wake with those from the controlled one is shown in Fig. 14. The base pressure in the controlled wake [Fig. 14(a)] is featured by a sharp pressure drop near the separation point and a significant base pressure recovery on the base. By comparing the pressure components in Figs. 16(b)–16(g), it is clear that the base-pressure recovery occurs due to a significant rise of $\overline{u}\partial\overline{v}/\partial x$ [Fig. 14(b)] and elimination of pressure from $\partial\overline{v'w'}/\partial z$ [Fig. 14(g)].

Figure 15 illustrates the 2D distribution of the major acceleration terms A_{Mx} and A_{Fy} and their respective key components $\partial\overline{v}/\partial x$ and $\overline{v'v'}$ on the x-y plane at $z/D = 0$. Consistent with the 3D distributions (Fig. 9), these two terms concentrate outside the separation streamline for both uncontrolled and controlled wakes.

In the uncontrolled case, A_{Mx} produces pressure gradients leading to low pressure in the recirculation and high pressure near the stagnation point, while A_{Fy} results in low pressure in the shear layer,

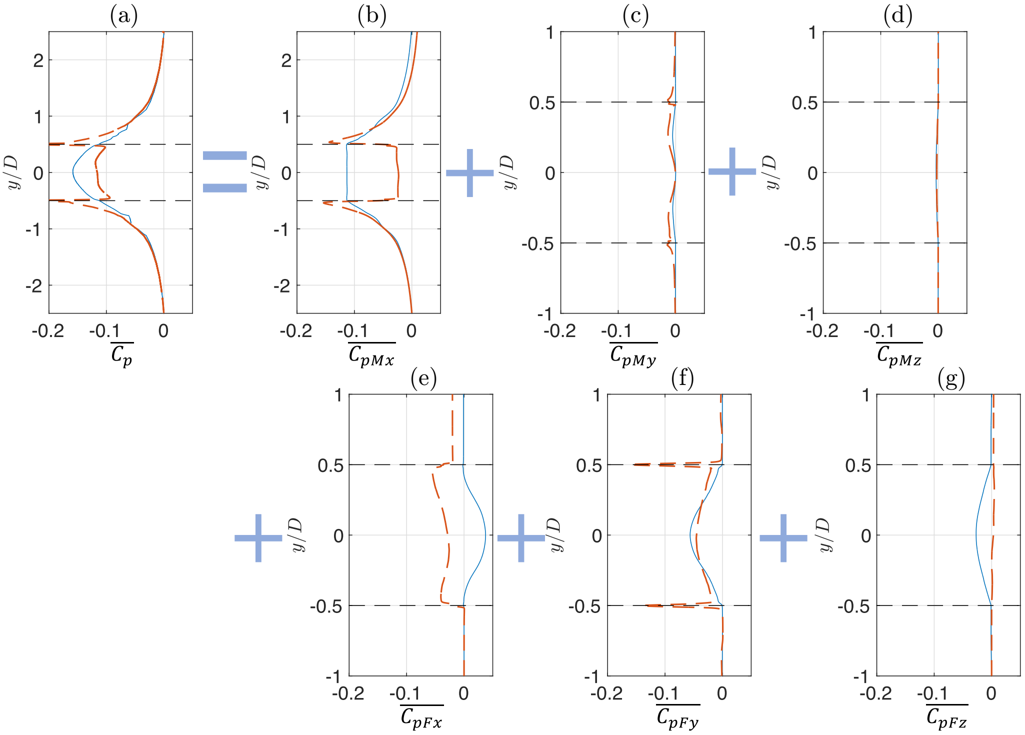

FIG. 14. The distribution of the pressure contribution from each momentum budget along the integration path ($x/D = 0.025$) for the uncontrolled wake (blue curve) and the controlled wake (red dashed curve). The black dashed lines mark the base edge ($y/D = \pm 0.5$).

near the stagnation point, and close to the base. Furthermore, as the deterministic component of A_{Mx}, the distribution of $\partial \overline{v}/\partial x$ [Fig. 15(c)] illustrates that the low pressure in the near wake is caused by the centripetal acceleration of the inlet flow toward the wake, corresponding to the concave separation streamline curvature. In the vicinity of the stagnation point, the centripetal deceleration of $\overline{v}$ with a convex separation streamline leads to a pressure rise. Directly resulting from $\overline{v'v'}$, Fig. 15(e) illustrates that the low pressure produced by A_{Fy} is consistent with the Reynolds normal stress $\overline{v'v'}$ distribution.

Near the base edge of the controlled wake, the deviation of the inlet flow toward the wake forms a concave separation streamline there, producing pressure gradients leading to pressure recovery [Figs. 15(b) and 15(d)]. In $\overline{v'v'}$ [Fig. 15(e)], although there exists a local pressure drop near the base edge due to the high Reynolds normal stress produced by the pulsed jet, the slight weakening of $\overline{v'v'}$ near the base results in higher base pressure.

As the dominating pressure source in the uncontrolled wake and the main factor leading to base-pressure recovery in the controlled one, the mean velocity term $\overline{u}\partial \overline{v}/\partial x$ is further discussed. This term originates from the streamwise convection of the lateral velocity component, corresponding to the centripetal acceleration of the inlet flow toward the wake, related to the streamline curvature of the mean flow. The streamwise velocity in this term is caused by the inlet flow, which is significant in the outer flow region but negligible near the base. The lateral velocity appears because of the centripetal acceleration of the inlet flow toward the base center, equivalent to a streamline curvature of the mean flow. In the controlled wake, most base-pressure recovery occurs near the base edge ($y/D = \pm 0.5$). This pressure rise is caused by the accelerated centripetal motion of the inlet flow

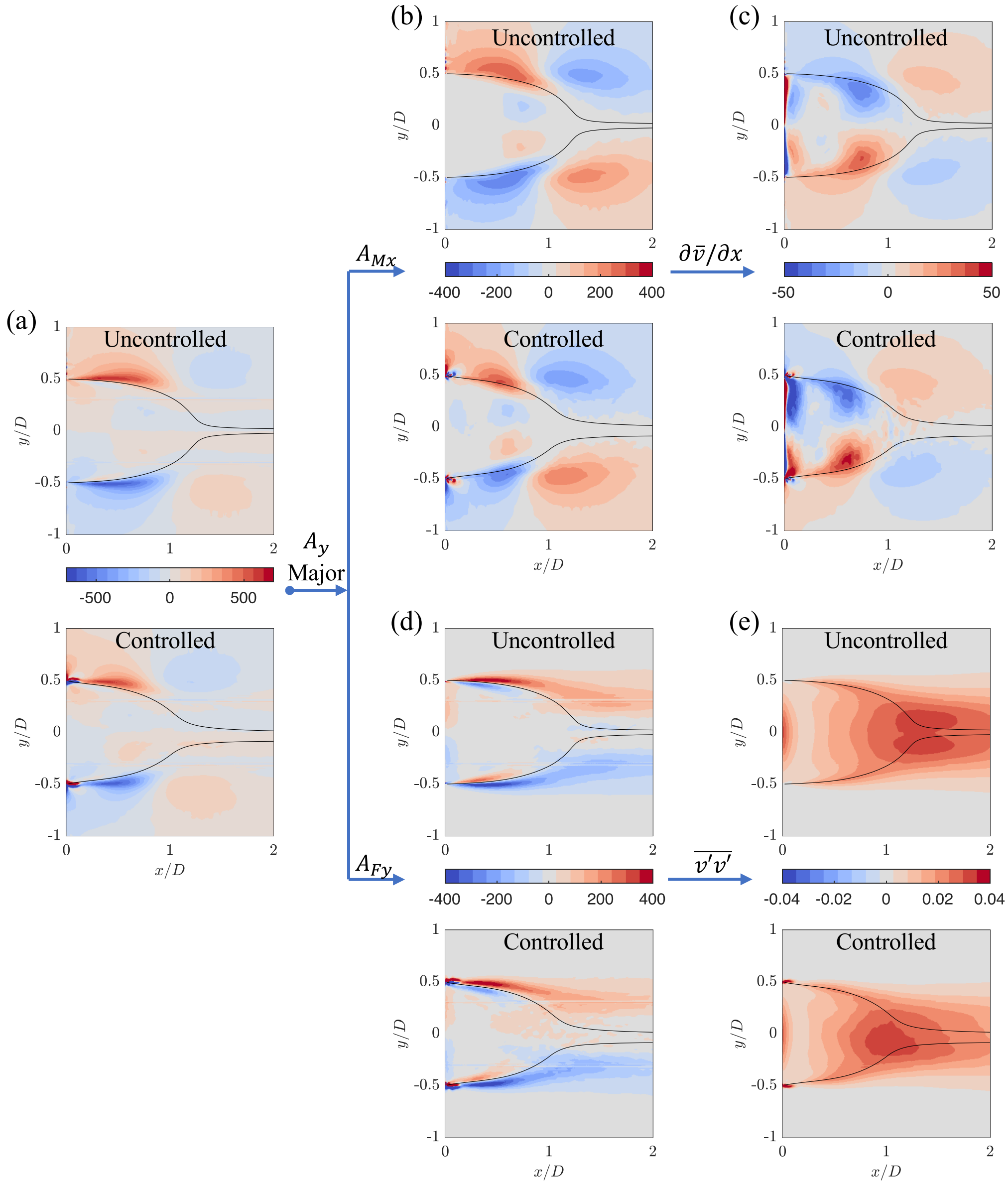

FIG. 15. A *x*-*y* slice view of (a) the *y* component pressure gradient, the major momentum budgets (b) A_{Mx} and (d) A_{Fy}, the term component (c) $\partial\bar{v}/\partial x$, and (e) $\overline{v'v'}$. In each subfigure, the upper side is the uncontrolled wake and the lower side is the controlled wake. The units of the pressure gradient are Pa/m. The black curve marks the separation streamline.

near the base edge, which manifests as local streamline curvature near the separation point [21], resulting in a global narrowing of the wake [21,28].

Based on $\partial\bar{v}/\partial x$, or more precisely, the streamline curvature after separation, three flow control scenarios are given in Fig. 16. Compared with the uncontrolled wake [Fig. 16(a)], elongating the wake [Fig. 16(b)] reduces the streamwise gradient of the lateral velocity, resulting in base-pressure recovery. In contrast, shortening the wake [Fig. 16(c)] causes base-pressure drop since $\partial\bar{v}/\partial x$ is

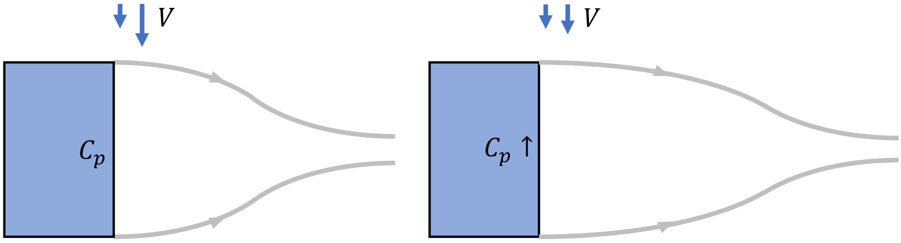

(a) Uncontrolled wake ($\partial\bar{v}/\partial x$ leads to low C_p)

(b) Elongate wake (decrease $\partial\bar{v}/\partial x$, C_p increases)

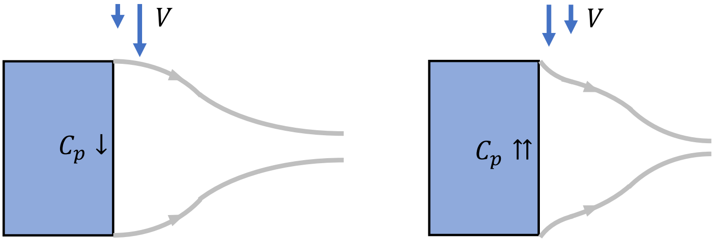

(c) Shorten wake (increase $\partial\bar{v}/\partial x$, C_p decreases)

(d) Reshape wake (reverse $\partial\bar{v}/\partial x$, C_p increases)

FIG. 16. A schematic of (a) the uncontrolled separation streamline and three flow control scenarios, including (b) the elongated wake, (c) the shortened wake, and (d) the reshaped wake. The gray curve shows the separation streamline. The blue arrow shows the lateral velocity component.

increased. By reshaping the wake [Fig. 16(d)], the effect of $\partial\overline{v}/\partial x$ on the base pressure can be reversed, resulting in a significant base-pressure rise. In the reshaped wake [Fig. 16(d)], although the wake length is shortened, an evident pressure increase can be achieved since the wake shape and the velocity distribution near the separation point are changed. These flow control scenarios are supported by our flow control results achieved both numerically with LES and experimentally with the wind tunnel experiment.

(1) *Scenario* (b). The turbulent wake was controlled by a traveling jet, which consists of a jet profile undergoing traveling motion along the base edge [38]. By applying a baseline near the base edge, a base-pressure recovery of $\Delta\overline{\langle C_p\rangle} = 0.078$ (62%) is observed. By comparison, a key difference between the uncontrolled flow and the controlled one is the elongation of the wake; the wake stagnation point location is increased by 40% in the controlled result, which agrees with the control scenario (b) proposed.

(2) *Scenario* (c). In the same numerical configuration analyzed in this section, when a low-frequency pulsed jet of 200 Hz is issued near the base edge, a base-pressure drop from $\overline{\langle C_p\rangle} = -0.125$ to $\overline{\langle C_p\rangle} = -0.14$ is observed [21]. In this flow control condition, it is observed that the curvature of the separation streamline increases, which shortens the wake and leads to a pressure drop from the mean velocity term $\partial\overline{v}/\partial x$.

(3) *Scenarios* (b) *and* (c). By simultaneous base-pressure and time-resolved Particle image velocimetry (PIV) measurement of the turbulent wake, the relationship between the wake length and the base pressure is analyzed with conditional averaging [24]. It illustrates that, even without any control, the turbulent wake undergoes transitions between high and low base-pressure conditions, which corresponds to different wake lengths (higher pressure with longer wake length).

(4) *Scenario* (d). By reshaping the turbulent wake with a high-amplitude, high-frequency pulsed jet, Zhu [48] demonstrated 88% overall base-pressure recovery, and near the base center, positive base pressure is achieved (136% pressure recovery at this position). In agreement with scenario (d), in the controlled wake, $\partial\overline{v}/\partial x$ produces a positive base-pressure contribution, resulting in a significant base-pressure rise.

Besides the streamline curvature effect, the momentum decomposition also identified key pressure contributions from the Reynolds stresses: in the uncontrolled wake, the effect of the Reynolds normal stress is to produce low pressure, while the Reynolds shear stress may lead to pressure recovery. This highlights an important implication for flow control: beyond managing streamline curvature, effective strategies may also target the fluctuating field—particularly the Reynolds normal stress, which produces a net negative pressure contribution. In the wake region, properly suppressing the unsteady flow motion may lead to pressure recovery due to the weakening of the Reynolds normal stress. Additionally, producing significant Reynolds normal stresses in front of a bluff body can induce a localized low-pressure region, potentially leading to significant pressure drag reduction or a net propulsion force.

VI. CONCLUSIONS

The momentum decomposition method provides a rigorous framework for attributing the pressure field to distinct physical mechanisms and quantifying their contributions via specific momentum budgets. These budgets can be classified into five fundamental types, each representing a key physical mechanism: (I) the streamline curvature effect (A_{Mx}, A_{Mz}); (II) convective acceleration (A_{My}); (III) Reynolds shear stresses (A_{Fx}, A_{Fz}); (IV) Reynolds normal stress (A_{Fy}); and (V) viscous diffusion (A_V). The central insight of this framework is that the pressure field arises from the inherent balance and compensation among these competing physical mechanisms. By decoupling their complex, intertwined effects in turbulent flow, the method enables a mechanistic and rationalistic analysis of pressure generation. Consequently, interpreting the pressure field reduces to understanding this intermechanism balance of momentum budget. This physics-based perspective is essential for fundamental flow diagnostics and, ultimately, forms a rigorous foundation for designing and analyzing targeted flow control strategies, as control actions can be rationally linked to the manipulation of specific momentum budgets.

The DNS results at $\mathrm{Re}_D = 200$ show that for flow around a cylinder, the pressure contributions from the mean velocity budget terms mainly manifest as a streamline curvature effect and flow accelerations. It contributes to a high-pressure region near the body front and low pressure on both sides of the object. From outside the near wake, the mean velocity budgets produce a pressure drop resulting in a low-pressure region in the recirculation bubbles, while further downstream, after the stagnation point, it leads to a pressure rise. In the wake region, the pressure gradient receives contributions from the fluctuating field terms due to the unsteady vortex shedding, especially the Reynolds normal stress, which leads to low pressure in the wake region. Despite the low Reynolds number in the DNS, the contribution from the viscous terms is very low compared with the other terms and mainly concentrates in the boundary layer near the body front, while their influence on the wake pressure field is negligible.

The low pressure in the turbulent wake at $\mathrm{Re}_D \approx 2 \times 10^5$ receives main contributions from outside it instead of inside, attributed to the streamline curvature effect of the potential inlet flow. The acceleration terms contributing to pressure variation can be further grouped into two regions.

(1) *Outer flow region* ($|y/D| \gtrsim 0.5$). In this region, the flow is largely potential, and the mean velocity term $\overline{u}\partial\overline{v}/\partial x$ dominates, contributing over 70% of the base pressure and ≈60% of global pressure. It manifests as the streamline curvature effect caused by the streamwise convection and centripetal acceleration of the inlet flow toward the wake. It indicates that most of the low pressure originates from outside the wake by the mean velocity field, closely related to the shape of the separation streamline.

(2) *Inner flow region* ($|y/D| \lesssim 0.5$). In this region, the pressure variation is mainly from Reynolds stresses, which are associated with the unsteady motion inside the wake.

(i) *Reynolds normal stress term* $\partial\overline{v'v'}/\partial y$. This term contributes the most base-pressure variation and becomes the second largest low base-pressure source (35% at most). The Reynolds normal stress directly reduces its local pressure since the integration $\int \partial\overline{v'v'}/\partial y \mathrm{d}y$ is equivalent to $\overline{v'v'}$.

(ii) *Reynolds shear stress term* $\partial\overline{u'v'}/\partial x$. Contrary to all the other terms, which decrease the base pressure, this term increases the base pressure by a maximum of 23%. It is ascribed to a curvature effect in the x-y plane of the fluctuating flow.

(iii) *Reynolds shear stress term* $\partial\overline{v'w'}/\partial z$. This term indicates the three-dimensional nature of the wake, providing a quantitative manner to evaluate the influence of the three-dimensionality of the wake on the base pressure. It takes up ≈10% of the base pressure.

The active control effect of the separated shear layer near the separation point is investigated, showing that the base-pressure recovery is linked to the pressure rise from $\overline{u}\partial\overline{v}/\partial x$, forming a concave streamline near the separation point. By analyzing the main base-pressure source $\overline{u}\partial\overline{v}/\partial x$, the separation streamline curvature caused by flow control can be linked to the base pressure, and a physical interpretation of three flow control scenarios is presented. In addition to the streamline curvature effect of the mean velocity terms, the momentum decomposition also illustrates that controlling the unsteady flow motions may contribute to drag reduction when the Reynolds stresses are favorably manipulated.

The above results provide a reference for analyzing the source of the pressure field in the wake and the development of the flow control method. The generic method proposed here may also apply to other geometries and datasets, under the condition that the NS equations are valid. Beyond the scope of this article, there exist several questions remaining to be investigated, such as the scaling law of the momentum budgets over different Reynolds numbers, geometries, and actuation; the application of the momentum decomposition to PIV experimental results; the development of flow control methods based on the momentum budgets, etc.

ACKNOWLEDGMENTS

This work was supported by the National Natural Science Foundation of China (Grants No. 52402451 and No. 52372360); the China Postdoctoral Science Foundation (Grant No. 2024M762406); the National Key R&D Program of China (Grant No. 2022YFE0208000); the Shanghai Key Laboratory of Aerodynamics and Thermal Environment Simulation for Ground Vehicles (Grant No. 23DZ2229029); and the Fundamental Research Funds for the Central Universities. The LES database was produced by the first author as part of his Ph.D. at Imperial College London [21,48].

The authors report no conflicts of interest.

DATA AVAILABILITY

The data that support the findings of this article are not publicly available upon publication because it is not technically feasible and/or the cost of preparing, depositing, and hosting the data would be prohibitive within the terms of this research project. The data are available from the authors upon reasonable request.

[1] G. Kirchhoff, Zur theorie freier flüssigkeitsstrahlen, J. Angew. Math. **1869**, 289 (1869).

[2] D. Riabouchinsky, On steady fluid motions with free surfaces, Proc. Lond. Math. Soc. **s2-19**, 206 (1921).

[3] T. Y. T. Wu, Cavity and wake flows, Annu. Rev. Fluid Mech. **4**, 243 (1972).

[4] V. V. Sychev, Asymptotic theory of separation flows, Fluid Dyn. **17**, 179 (1982).
[5] A. Roshko, Perspectives on bluff body aerodynamics, J. Wind Eng. Ind. Aerodyn. **49**, 79 (1993).
[6] S. Balachandar, R. Mittal, and F. M. Najjar, Properties of the mean recirculation region in the wakes of two-dimensional bluff bodies, J. Fluid Mech. **351**, 167 (1997).
[7] J. L. Lumley, *Stochastic Tools in Turbulence* (Academic Press, New York, 1970).
[8] P. J. Schmid, Dynamic mode decomposition of numerical and experimental data, J. Fluid Mech. **656**, 5 (2010).
[9] O. T. Schmidt, A. Towne, G. Rigas, T. Colonius, and G. A. Brès, Spectral analysis of jet turbulence, J. Fluid Mech. **855**, 953 (2018).
[10] A. Towne, O. T. Schmidt, and T. Colonius, Spectral proper orthogonal decomposition and its relationship to dynamic mode decomposition and resolvent analysis, J. Fluid Mech. **847**, 821 (2018).
[11] B. R. S. Freeman, R. J. Martinuzzi, and A. Hemmati, Exploring the influence of span-wise boundary conditions on the wake of a thin flat plate using Fourier-averaged Navier–Stokes equations, Int. J. Heat Fluid Flow **103**, 109176 (2023).
[12] B. R. S. Freeman, R. J. Martinuzzi, and A. Hemmati, Momentum analysis of complex time-periodic flows, J. Fluid Mech. **979**, A50 (2024).
[13] M. Grandemange, M. Gohlke, and O. Cadot, Turbulent wake past a three-dimensional blunt body. Part 1. Global modes and bi-stability, J. Fluid Mech. **722**, 51 (2013).
[14] H. Choi, J. Lee, and H. Park, Aerodynamics of heavy vehicles, Annu. Rev. Fluid Mech. **46**, 441 (2014).
[15] G. Rigas, A. S. Morgans, R. D. Brackston, and J. F. Morrison, Diffusive dynamics and stochastic models of turbulent axisymmetric wakes, J. Fluid Mech. **778**, R2 (2015).
[16] G. Pavia, M. Varney, M. Passmore, and M. Almond, Three dimensional structure of the unsteady wake of an axisymmetric body, Phys. Fluids **31**, 025113 (2019).
[17] L. Dalla Longa, O. Evstafyeva, and A. S. Morgans, Simulations of the bi-modal wake past three-dimensional blunt bluff bodies, J. Fluid Mech. **866**, 791 (2019).
[18] Y. Fan, C. Xia, S. Chu, Z. Yang, and O. Cadot, Experimental and numerical analysis of the bi-stable turbulent wake of a rectangular flat-backed bluff body, Phys. Fluids **32**, 10511 (2020).
[19] K. He, G. Minelli, X. Su, G. Gao, and S. Krajnović, On state instability of the bi-stable flow past a notchback bluff body, J. Fluid Mech. **931**, R6 (2022).
[20] V. Gentile, F. F. J. Schrijer, B. W. Van Oudheusden, and F. Scarano, Low-frequency behavior of the turbulent axisymmetric near-wake, Phys. Fluids **28**, 065102 (2016).
[21] T. Zhu and J. F. Morrison, Simulation of the turbulent axisymmetric bluff body wake with pulsed jet forcing, Phys. Rev. Fluids **6**, 124604 (2021).
[22] M. Grandemange, M. Gohlke, and O. Cadot, Bi-stability in the turbulent wake past parallelepiped bodies with various aspect ratios and wall effects, Phys. Fluids **25**, 095103 (2013).
[23] R. D. Brackston, J. M. García de la Cruz, A. Wynn, G. Rigas, and J. F. Morrison, Stochastic modelling and feedback control of bistability in a turbulent bluff body wake, J. Fluid Mech. **802**, 726 (2016).
[24] T. Zhu, G. Rigas, and J. F. Morrison, Near wake coherent structures of a turbulent axisymmetric bluff body wake, Int. J. Heat Fluid Flow **112**, 109668 (2025).
[25] G. Rigas, L. Esclapez, and L. Magri, Symmetry breaking in 3D wakes, in *Proceedings of the Summer Program, Center for Turbulence Research* (Stanford University, Stanford, 2016).
[26] H. Choi, W.-P. Jeon, and J. Kim, Control of flow over a bluff body, Annu. Rev. Fluid Mech. **40**, 113 (2008).
[27] M. C. Thompson, T. Leweke, and K. Hourigan, Bluff bodies and wake–wall interactions, Annu. Rev. Fluid Mech. **53**, 347 (2021).
[28] A. R. Oxlade, J. F. Morrison, A. Qubain, and G. Rigas, High-frequency forcing of a turbulent axisymmetric wake, J. Fluid Mech. **770**, 305 (2015).
[29] D. Barros, J. Borée, B. R. Noack, A. Spohn, and T. Ruiz, Bluff body drag manipulation using pulsed jets and Coanda effect, J. Fluid Mech. **805**, 422 (2016).
[30] Y. Haffner, J. Borée, A. Spohn, and T. Castelain, Unsteady Coanda effect and drag reduction for a turbulent wake, J. Fluid Mech. **899**, A36 (2020).

[31] D. Fan, B. Zhang, Y. Zhou, and B. R. Noack, Optimization and sensitivity analysis of active drag reduction of a square-back Ahmed body using machine learning control, Phys. Fluids **32**, 125117 (2020).

[32] T. Shaqarin, P. Oswald, B. R. Noack, and R. Semaan, Drag reduction of a D-shaped bluff-body using linear parameter varying control, Phys. Fluids **33**, 077108 (2021).

[33] Y. Haffner, T. Castelain, J. Borée, and A. Spohn, Manipulation of three-dimensional asymmetries of a turbulent wake for drag reduction, J. Fluid Mech. **912**, A6 (2021).

[34] B. F. Zhang, D. W. Fan, and Y. Zhou, Artificial intelligence control of a low-drag Ahmed body using distributed jet arrays, J. Fluid Mech. **963**, A3 (2023).

[35] T. J. Lambert, B. Vukasinovic, and A. Glezer, Aerodynamic flow control of axisymmetric bluff body by coupled wake interactions, AIAA J. **56**, 2992 (2018).

[36] T. J. Lambert, B. Vukasinovic, and A. Glezer, A freely yawing axisymmetric bluff body controlled by near-wake flow coupling, J. Fluid Mech. **863**, 1123 (2019).

[37] T. J. Lambert, B. Vukasinovic, and A. Glezer, Fluidic control of a precessing axisymmetric body by near-wake coupling, Phys. Rev. Fluids **9**, 053904 (2024).

[38] A. Canova, T. Zhu, and J. F. Morrison, Control of a bluff body wake using travelling jets, Int. J. Heat Fluid Flow **110**, 109605 (2024).

[39] G. Rigas, A. R. Oxlade, A. S. Morgans, and J. F. Morrison, Low-dimensional dynamics of a turbulent axisymmetric wake, J. Fluid Mech. **755**, R5 (2014).

[40] P. M. Nadge and R. N. Govardhan, High Reynolds number flow over a backward-facing step: Structure of the mean separation bubble, Exp. Fluids **55**, 1657 (2014).

[41] B. Podvin, S. Pellerin, Y. Fraigneau, G. Bonnavion, and O. Cadot, Low-order modelling of the wake dynamics of an Ahmed body, J. Fluid Mech. **927**, R6 (2021).

[42] C. Zhang, Mechanisms for aerodynamic force generation and flight stability in insects, Ph.D. thesis, Johns Hopkins University, 2015.

[43] K. Menon and R. Mittal, On the initiation and sustenance of flow-induced vibration of cylinders: Insights from force partitioning, J. Fluid Mech. **907**, A37 (2021).

[44] S. Prakhar, J.-H. Seo, and R. Mittal, Modal force partitioning–a method for determining the aerodynamic loads for decomposed flow modes with application to aeroacoustic noise, J. Fluid Mech. **1013**, A7 (2025).

[45] P. Bradshaw and Y. M. Koh, A note on Poisson's equation for pressure in a turbulent flow, Phys. Fluids **24**, 777 (1981).

[46] T. Zhu, Y. Pan, and J. Morrison, Numerical simulation of the pressure characteristics of the pulsed jet actuator, Aeronaut. J. **128**, 896 (2024).

[47] S. Davoust, L. Jacquin, and B. Leclaire, Dynamics of $m = 0$ and $m = 1$ modes and of streamwise vortices in a turbulent axisymmetric mixing layer, J. Fluid Mech. **709**, 408 (2012).

[48] T. Zhu, The turbulent axisymmetric bluff body wake: Analysis and control through experiment and simulation, Ph.D. thesis, Imperial College London, 2023.